An Examination of MHz Rate PIV in a Heated Supersonic Jet

by

Bryan Brock

A thesis submitted to the Graduate Faculty of
Auburn University
in partial fulfillment of the
requirements for the Degree of
Master of Science

Auburn, Alabama
August 2, 2014

Keywords: PIV, Aeroacoustics, Jet Noise

Copyright 2014 by Bryan Brock

Approved by

Brian Thurow, Chair, Associate Professor of Aerospace Engineering
Roy Hartfield, Professor of Aerospace Engineering
Andrew Shelton, Assistant Professor of Aerospace Engineering

Abstract

An experimental investigation of a high temperature, supersonic jet conducted at the University of Mississippi's National Center for Physical Acoustics is described. Time-resolved particle image velocimetry (PIV) was used in the acquisition of flow field velocity measurements eight inches downstream of a two inch axissymmetric supersonic nozzle operating at a Mach number of 1.56 and total temperature of $1350°F$. A MHz rate gate-intensified CCD framing camera was used in conjunction with a pulse-burst laser system in the acquisition 308 image sequences. Each sequence consisted of 16 images with a temporal spacing of $1\mu s$ between each frame. A background on high-speed measurement techniques and jet aeroacoustics as well as the experimental setup, operational conditions, and experimental results involving the velocity field are described in detail. A number of experimental hurdles had to be overcome in order to increase the data quality. These include the construction of a sound insulating box to prevent image blurring caused by the high acoustic levels within the test environment, the alignment of the Cordin's eight internal cameras to ensure one optical path, and the reduction of noise inherent to the Cordin's images through various filtering methods. The velocity fields were obtained through the use of standard PIV analysis as well as High Dynamic Range (HDR) PIV using dynamic evaluation via ordinary least squares (DEVOLS) algorithm. Proper orthogonal decomposition (POD) was used to reconstruct the velocity fields in order to improve their quality. This method was successful in eliminating much of the noise remaining in the velocity fields. Time resolved velocity sequences are displayed to show the characteristics of the turbulent shear layer in the supersonic jet. The average acceleration fields are shown are poor in quality due to various experimental obstacles.

Acknowledgments

The work encompassed within this thesis is the culmination of my graduate career which I would not have been able to complete without the support, encouragement and guidance of a number of people who I would like to acknowledge for their efforts.

First and foremost I would like to thank Dr. Brian Thurow for giving me the opportunity and guidance to see me through my academic career at Auburn. His passion for education and research has challenged me to continually strive to meet the high standards that is Auburn Engineering. Without his effort I would not be where I am today.

Dr. Nathan Murray, Greg Lyons and the rest of the aeroacoustics group at the Jamie Whitten National Center for Physical Acoustics, for their time and efforts in assisting during my stay in Oxford, Mississippi. This thesis would not have been possible without their hospitality and support.

Dr. Roy Hartfield for his incredible contribution not only to my academic career but also for his efforts and support in helping me to find direction in life after Auburn. His dedication to his students education has had a profound impact on my understanding of the field of aerospace engineering.

To the rest of the Auburn Aerospace Engineering faculty that have given me the knowledge and tools over the past six years to leave Auburn and enter the workforce with confidence and a firm understanding of the fundamental aspects of aerospace engineering.

Finally to my parents, Fred and Sandra Brock and my wife Meredith Brock for their continual love and encouragement throughout my education. Without their unwavering support and patience I could have never succeeded. While the paths ahead are unknown, I know none will be too difficult with them by my side.

Table of Contents

List of Figures

List of Tables

Chapter 1

Introduction

The onset of the jet age in the 1950's and 60's revolutionized the aviation industry and brought about new areas of research throughout the field of aerospace engineering. One such area is the field of aeroacoustics which involves analyzing the generation and propagation of sound in fluid flows with the hopes of reducing noise. This was spurred forward by the fact that jet aircraft were generating more sound pollution than ever. The field saw considerable growth in these two decades, led by pioneers such as Lighthill. As the name implies, aeroacoustics falls between the fields of aerodynamics and acoustics, drawing heavily from both. Its central goal, as defined by Rogers is "to define an acoustic analogy, by which the real problem of the noise radiated by a rotor and/or a highly disturbed flow is replaced by the classical acoustic radiation in a medium at rest with equivalent acoustic sources."[7] A detailed explanation of the sources of sound and the sound generating mechanisms within jet flows can be found in Chapter 2.

The early years of aeroacoustics saw major advances in the development of its fundamental theory. However, like any branch of fluid mechanics, aeroacoustics presents a challenging problem analytically due to our inability to fully solve its governing equations. As is often done the focus of research was shifted to the use of experimental methods as a means of gaining a more fundamental understanding of the mechanisms for sound generation within a fluid flow. This approach however was limited for a number of years by the technological limitations of the 50's, 60's, and 70's.

In recent years with the continued development and advances in experimental techniques and their technologies, the examination of the sound generating mechanisms in complex flows, such as supersonic jets, has become possible. Supersonic aeroacoustics has historically

relied on intricate microphone arrays as a method of locating and identifying sound sources. While these arrays are still implemented, the development of high speed, high-resolution digital cameras within the past twenty years has allowed for the use of particle image velocimetry (PIV) as well. In the past the use of PIV in high-speed flows has been hindered by the necessary camera frame rates and resolution as well as limitations in high speed lasers. The advances in technology have not only increased the use of standard PIV on high speed flows, but have also allowed the implementation of other techniques such as time-resolved PIV which can measure velocity and acceleration.

The scope of this thesis covers the acquisition and examination of the PIV data gathered in a joint research project involving Auburn University, University of Mississippi, and University of Texas. This project is sponsored by the Office of Naval Research (ONR) through their Jet Noise Reduction (JNR) program. The Navy has a particular interest in the reduction of jet noise due to the close interaction of Navy personnel with jet aircraft. The noise generated by the Navy's low bypass turbofan engines on aircraft carrier decks has resulted in hearing loss in some of the flight deck personnel. The benefits that would stem from the ability to effectively reduce jet noise extends beyond the military to civilian uses, such as decreased sound pollution around airports and a reduction in air frame structural degradation. While the scope of this project is wide ranging, including both near field and far field pressure data as well as streak images taken on a PCO edge camera, the focus of this thesis will be on the time resolved velocity data gathered in the second year of the program. A number of obstacles were encountered during the acquisition of the PIV data due to the harsh test environment and the Cordin camera. These include image blurring due to high acoustic levels, misalignment of internal camera optics, large levels of image noise due to intensified affects and finally low particle seeding within the imaged region. To overcome these complications, a unique methodology for the processing of time-resolved data was developed and will be discussed at length in this thesis. This work was preceded in the previous year by

Harris Haynes who has now graduated from Auburn University. Much of the ground work for this thesis was laid by him during the first year of the project. [8]

Chapter 2

Aero-Acoustic Background

2.1 Background

General acoustics refers to the the physics of sound, its generation, and how it propagates through a medium. Sound is caused by changes in density over time which are emitted in the form of waves. When referring to sound waves, they are often described in terms of wavefronts, which are sound waves, or density fluctuations, that are equal in phase. These wavefronts form lines or surfaces that propagate together.[1] While fluctuations in density is one way of describing sound, pressure fluctuations is often used instead. This is possible because density and pressure are intimately related through the equation of state. An example of this is the wave equation:[7]

$$\Delta p' - \frac{1}{a_0^2}\frac{\partial^2 p'}{\partial t^2} = 0 \quad \text{or} \quad \frac{\partial^2 p'}{\partial t^2} - a_0^2 \frac{\partial^2 p'}{\partial x_i^2} = 0 \quad \text{or} \quad \frac{\partial^2 \rho}{\partial t^2} - a_0^2 \bigtriangledown^2 \rho = 0 \tag{2.1}$$

which describes sound waves in terms of a pressure field for a homogeneous medium at rest. While this may describe a known sound field, it gives no information regarding the mechanism for its generation which is a chief concern in aeroacoustics. For this reason the generation of sounds and their sources is explained below.

2.1.1 Sources of Sound

When discussing aeroacoustics, it is important to first describe the different sources of sound and how they are generated. The different sounds we hear on a day to day basis fall into three separate categories which are displayed in Figure 2.1 below. Lightill summed

these up these up nicely in his classic paper *On Sound Generated Aerodynamically I* in which he described these three ways in which sound is generated:

1. "By forcing the mass in a fixed region of space to fluctuate.

2. By forcing the momentum in a fixed region of space to fluctuate.

3. By forcing the rates of momentum flux across fixed surfaces to vary."[9]

While this description may be clear to readers with a background in acoustics, a more in depth explanation may be required for some readers and is given below.

The first, and most easily understood category of sound sources are those generated through the the displacement of fluid through an unsteady process. Category 1 sounds also impart a net force on the fluid and are described by the acceleration of the volume of the fluid, meaning how fast the rate of the volume displacement is changing. While this may seem obscure, practical descriptions of such sources are not; which include sirens, direct radiator loud speakers, and vibrating surfaces. These sound sources are considered the most efficient, meaning the ratio of generated sound to the energy required to produce it is higher than those of other sources.[1] A depiction of a category 1 sound is shown at the top of Figure 2.1.

The second category of sound sources can be difficult to describe in physical terms but is one of the most important sources of noise generated in the aerospace field. Category 2 sources are those which produce a net force on a fluid without generating a net displacement within the fluid's volume. It is most easily visualized as the interaction of a moving fluid with a rigid body, or vice-versa. The noise created by such sources is due to the exchange of kinetic energy to sound which occurs when the fluid interacts with a solid body. Category 2 noise is focus point of much research within aeroacoustics due to its affect on noise pollution in populated areas. Examples of such includes the noise generated by the passing of high speed trains and by the turbulent flow of air around the landing gear on commercial aircraft. [1]

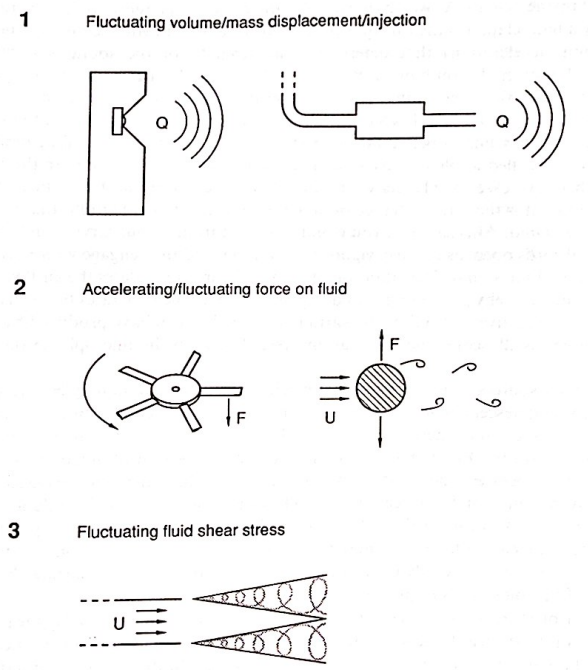

Figure 2.1: Three Catagories for Sound Sources[1]

Category 2 sources can also be described through the separation of flow behind a cylinder. This unsteady, periodic motion creates a random broadband noise due to the turbulence within the flow. Broadband noise refers to a sound which covers a wide range of frequencies. The noise generate by rotor craft and propellers can also be attributed to this turbulent noise. For instance the interaction of a blade with the turbulent vortex shed from the tip of the preceding blade generates a loud "clap" sound which is called blade-vortex interaction. These are depicted in the center of Figure 2.1.

The third and final category of sound sources is the one most prevalent to this work. Category 3 sources have both a zero net volume displacement and zero net force on the fluid. Instead its production of sound waves is caused by the fluctuating stress on the fluid. The sound generated by category 3 sources is highly inefficient because fluids are poor supporters of shear stress.[10] Because this noise is due to the presence of fluid shear stress, it is most commonly found in where shear layers are present between fluids moving at different velocities. The most apparent example of this is the noise generated by the turbulent mixing

when a high speed jet is a ejected into relatively stationary fluid.[1] The bottom of Figure 2.1 depics this scenario.

While we now have a physical description, or qualitative description of the three different categories of sound sources, we are no closer to understanding them in a quantitative manner. This however is addressed by representing each of these as a mathematical source, or mode of oscillation. Category 1 sources can be represented by a monopole, which emits sound equally in all directions. This satisfies the criteria for a category 1 source because there is both a volume displacement and force acting on the fluid. The monopole is often referred to in aeroacoustics as the "source term" as will be shown later. Category 2 can be described as a dipole. A dipole is simply two monopoles a very short distance apart which have an equal source strength but opposite phase. Because the two monopoles act in opposite phase, one monopole is essentially displacing fluid out while the other displaces fluid in. This satisfies our description of a category 2 source because there is no net fluid displacement, only a net force acting on the fluid. The third and final category is represented by a quadrupole, which is simply two dipoles of the same strength placed very close together and acting in opposite phase. The equations for these three modes of oscillation are listed:

$$\text{Monopole: } \mathbf{M} = \frac{1}{4\pi}\frac{\partial}{\partial t}\int_s \left[\frac{\rho_\infty V_i n_i}{R|1 - Mcos(\phi)}\right]_{t_e} dS \tag{2.2}$$

$$\text{Dipole: } \mathbf{D} = \frac{1}{4\pi}\frac{\partial}{\partial r_i}\int_s \left[\frac{(p - p_\infty) n_i}{R|1 - Mcos(\phi)}\right]_{t_e} dS \tag{2.3}$$

$$\text{Quadrupole: } \mathbf{Q} = \frac{1}{4\pi}\frac{\partial^2}{\partial r_i r_j}\int_V \left[\frac{T_{ij}}{R|1 - Mcos(\phi)}\right]_{t_e} dr_s \tag{2.4}$$

The components of these equations, more specifically Eq. 2.4 will be presented later in the thesis.

An important aspect of Eqs. 2.2-2.4 is that the intensity of each scales differently with velocity. The monopole, while the most efficient, only scales as the fourth power of velocity. The dipole, while less efficient, scales as the sixth power of velocity. Lastly the quadrupole's intensity scales to the eighth power of velocity. It is for this reason that it is

the primary source of sound in high speed turbulent jets despite its inefficiencies.[11] These three sources, and in particular the quadrupole, played an important role in the description of sound generation developed by Lighthill using the acoustic analogy which is presented in the following section.

2.2 Lighthill's Analogy

While it is possible to solve the wave equation shown above in Eq. 2.1 for simplified or very specific cases, arriving at a solution for arbitrary flows encountered in practical engineering applications is much more difficult. By "arbitrary flow" it is meant that the base flow isn't propagating through a uniform medium and isn't at rest.[7] As a result, Eqs. 2.2-2.4 become coupled and cannot be solved through the classical acoustic approach. This problem is addressed by introducing an acoustic analogy where the goal is to clearly distinguish between the sound due to radiation and fluid dynamics.[12] This is achieved by representing the sound field with an equivalent one composed of the acoustic sources introduced above.[7] This process was pioneered by Lighthill in the 1950's and is by many considered the creator of the aeroacoustics field. His analogy, described below is the foundation of nearly all work pertaining to the field of aeroacoustics and is still heavily relied upon today.

Lighthill in the 1950's had the idea to rewrite the Navier Stokes Equations so that he could derive a wave equation.[7] This was done by writing the exact form of the momentum equation for a flow in any continuous medium.[9] This solution is known as Lighthill's equation:

$$\frac{\partial^2}{\partial t^2} - a_0^2 \bigtriangledown^2 \rho = \frac{\partial^2 T_{ij}}{\partial x_i \partial x_j} \tag{2.5}$$

where a_0 is the speed of sound within the medium, and ρ is its density. Also represented in the equation by T_{ij} is Lighthill's stress tensor which is defined as:

$$T_{ij} = \rho U_i U_j + (p - \rho a_0^2)\partial_{ij} - \tau_{ij} \tag{2.6}$$

where $\rho U_i U_j$ represents the Reynolds stress and τ_{ij} is the viscous stress tensor. The middle term in Eq. 2.6 accounts for any effects due to non-uniform entropy. [7]

These equations represent an exact solution for the propagation of sound through a uniform medium at rest. It is important to note that the left hand side of the equation takes on the form of the wave equation written in terms of density (Eq. 2.1) and represents the entire acoustic field. This equation however is not without its difficulties, which comes in the form of the double divergence of the Lighthill stress tensor in Eq. 2.6 which cannot be solved in its current form. In the field of aerodynamics, as noted by Lighthill, the flow can be assumed to have a high Reynolds Number, at which point the inertial forces within the flow dominate, with little effect from the viscous forces allowing for the viscous stress term to be neglected. Also by assuming isentropic flow, the middle term can be dropped out. Finally, if the flow is considered incompressible, then the fluctuating velocity components, U_i' and U_j', within U_i and U_j can be ignored and Eq. 2.6 becomes:

$$T_{ij} \approx \rho_0 \bar{U}_i \bar{U}_j \tag{2.7}$$

where the components $\bar{U}_i$ and $\bar{U}_j$ represent the mean velocity components of the flow field.[9] This now represents an incompressible approximation for the real flow which can be used in the evaluation of the acoustic field. It is important to note that these equations represent sound produced by a quadrupole field, or purely aerodynamic noise. As discussed earlier, the contribution of the monopole, and dipole to the overall sound field can be large and are neglected in Lighthill's solution.

2.3 Turbulent Jet Noise

When examining turbulent jet noise with regards to its generation and propagation, one must first study the turbulent aspects of unsteady jet flow. The turbulence produced by these jet flows is a product of the mixing between high speed and low speed flows. This

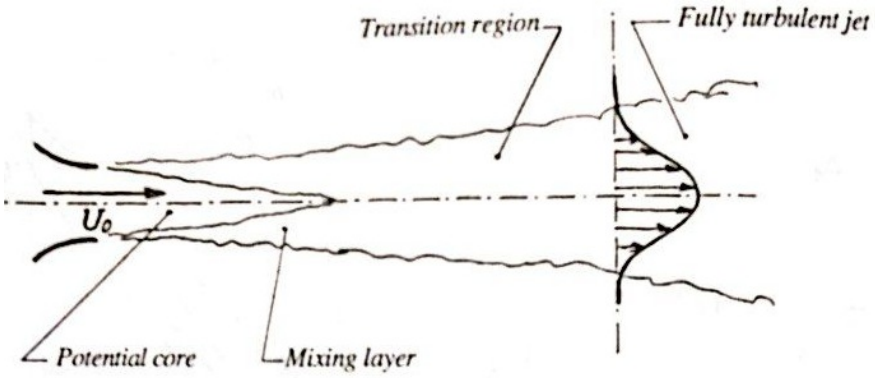

Figure 2.2: Axisymmetric Subsonic Jet Flow

is commonly found in many test apparatuses where a stationary nozzle is exhausting into a static atmosphere. The large velocity gradients produced by such flows results in a strong shear layer leading to turbulent flows.[7] A diagram of this can be sen in Figure 2.2. At the exit of the nozzle the high speed flow is uniform and there exists a laminar shear layer.[13] This shear layer is due to the large velocity gradient near the edge of the jet. The region labeled as the potential core represents the inner boundary of the mixing region where there doesn't exist a fluctuating quantity of the velocity. The potential core will typically stretch 4-6 nozzle diameters downstream of the nozzle exit.[14] The shear layer grows rapidly due to its instability and generates large scale vortical structures that entrains the ambient fluid and carrying it downstream. These large scale structures, or eddies are one source of the aerodynamic noise produced by a turbulent jet Which will be discussed in greater detail later in the paper. Approximately thirty jet diameters downstream the flow completes it's transition and consists of fully turbulent flow. The acoustical properties of these regions are complex and can be difficult to describe. However some methods have been developed which are capable of predicting the sound radiated by through the free shear layer.

2.3.1 Dimensional Analysis

Through the expansion of Lighthill's theory, various equations have been derived to describe the intensity of a sound field generated through turbulent mechanisms throughout

the flow and are listed below.

$$R_{pp}(\hat{x},\tau) = \frac{x_i x_j x_k x_l}{16\pi^2 \rho_0 {a_0}^5 x^6} \int \left(\frac{1}{1 - M_c cos(\theta)}\right)^5 \left\{ \frac{\partial^4}{\partial \tau' 4} \int R'_{ijkl}(\hat{y}, \hat{\xi}, \tau' + \frac{\hat{x}}{x} \times \frac{\hat{\xi}}{a_0(1 - M_c cos(\theta)}) \partial\hat{\xi} \right\}_{\tau' = \frac{\tau}{1 - M_c cos(\theta)}} \tag{2.8}$$

Equation 2.8 represents the autocorrelation function which if evaluated at $\tau = 0$, then the total intensity from the observation point can be calculated:

$$I(\hat{x}) = R_{pp}(\hat{x}, 0) \tag{2.9}$$

The density can also be solved for and is given by:

$$S_{pp}(\hat{x},\omega) = \frac{\pi\omega^4 x_i x_j X_k x_l}{2\rho_0 {a_0}^4 x^6} \int H_{ijkl}(\hat{y}, \frac{\omega}{a_0}\frac{\hat{x}}{x}, \omega(1 - M_c cos(\theta))\partial\hat{y} \tag{2.10}$$

A full explanation of these equations will not be given but it is clear simply from observation that these equations are extremely complex and difficult to solve. It is for this reason that dimensional analysis is required to arrive at applicable solutions.[7] The following process was outlined by Roger in *Turbulence and Jet Noise*. By applying some dimensional arguments to Eq. 2.8 where U_0 is the characteristic velocity, and D is the length scale in terms of the jet diameter, then a time scale for the large scale motion can be expressed as D/U_0. Also if the eddies are considered to be acoustically small, then each eddy is acoustically independent. Therefore by summing the intensities of all the eddies within the jet, the total intensity of the flow can be represented. From this it can be shown that the double integral of Eq. 2.8 scales as the volume of the jet squared.[7] Because the length scale is represented by D, the double integral is revealed to be proportional to D^6. Finally by letting the order of magnitude of the correlation tensor be equal to $\rho_0^2 U_0^4$ and evaluating the intensity at $\hat{x} = (R, \theta)$, Eqs. 2.8

and 2.9 reduce to:

$$I(\hat{x}) = K\frac{\rho_0 D^2}{a_0^5 R^2}\frac{U_0^8}{(1 - M_c cos(\theta))^5} \tag{2.11}$$

where R is some distance downstream and K is a constant. The most important component of Eq. 2.11 is the velocity term, U_0^8, which shows that the intensity of the of the acoustic field scales to the eighth power of velocity.[15] This confirms Lighthill's assertion that aeroacoustic noise is quadrupole in nature and that for high speed flows, this mechanisim of sound generation is efficient. This also explains why early turbojets and low-bypass turbofans produced so much noise whose method of thrust generation consisted of moving small quantities of air at very high rates. Today's high-bypass turbofans, while also being more efficient, are also quieter due to their process of moving very large quantities of air at lower velocities.[7] In the following section the effects of these high speed supersonic jets will be presented.

The scaling law described above, however, is only applicable to subsonic flows and breaks down at supersonic speeds. If applied to supersonic flows, this scaling method would predict that 100% of the jets power would be converted to the generation of noise which is an unrealistic prediction.[16] Instead it has been found through experimental investigations that the relationship between velocity and noise varies at supersonic speed. It was found by Sutherland[17] that for a Mach range of $M = 1$ to 1.5, the sound level scales with U^6. At even higher velocities with a range of $M > 1.5$ and $M \leq 2.5$, the sound level scales with U^4. Finally for Mach numbers greater than 2.5, it was found that the sound level is dependent on U^3. Because the scaling remains constant at these higher Mach numbers ($M > 2.5$), it is reasonable to assume that the efficiency of the sound generating mechanisms is independent of the jet velocity.[16] For the remainder of this paper, these sound generating mechanisms within supersonic jets will be explored.

2.4 Supersonic Jet Noise

Most of the information presented thus far has referred to the noise generated aerodynamically in subsonic jets. However, when addressing supersonic jet noise, the characteristics of the noise generation is considerably different and very complex, but for the most part are better understood and easier to predict.[2] There are various characteristics of supersonic jet noise, but it is widely believed that it is the large scale structures within supersonic flows that are responsible for the generation of noise by means of the turbulent shear layer. This is due to the movement of these large scale structures downstream at supersonic speeds which generates Mach wave radiation, or turbulent mixing noise. There is also often the presence of shock waves within the flows, which generate both screech tones and broadband-shock associated noise.[2] These three mechanisms comprise the the methods in which noise is generated for supersonic jets. Each will be discussed below; however, before moving on, it is interesting to note that while it is now readily believed that the large scale motions are responsible for a large portion of the sound generated in supersonic jets, it but not entirely clear if the small scale motions within subsonic jets are responsible for sound generation. This topic is an ongoing debate which will not be fully determined without more extensive experimentation.

2.4.1 Turbulent Mixing Noise

Two sources of sound generated by turbulent mixing exist in jet flows. The first source is due to the presence of large scale turbulent structures within the flow. This source is dominant at high subsonic or supersonic Mach numbers and acts primarily in the down stream direction corresponding to the emission of a Mach wave. The method in which turbulent mixing generates noise is explained by replacing the large turbulent structures with a wavy wall depicted in Figure 2.3. The wavy wall is considered to be of the same wave speed and wavelength as the instabilities within the flow. Because the ambient air located above the wavy wall is subsonic while below it exists supersonic flow, a Mach wave is emitted

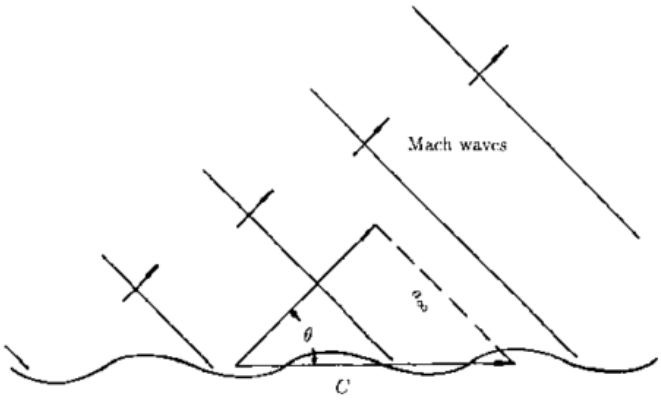

Figure 2.3: Wavy Wall Approximation for Turbulent Jet[2]

which generates a significant amount of noise. This also suggests that the intensity of the radiating sound is dependent on the angle at which the mach wave is emitted. This angle has been found to be dependent on the Mach number of the jet as well as its temperature.[2] The second source of turbulent mixing noise is due to fine scale turbulence and radiates in all directions, however it is dominant in the sideline and upstream direction.[18] It was also found that temperature exerts a complex effect on the noise generated by turbulent mixing within supersonic jets. Tam found in *Fine-Scale Turbulence Noise from Hot Jets*[18], that hot jets are more dynamically unstable with a higher turbulent kinetic energy. This increase in turbulent kinetic energy due to instabilities is counteracted by a decrease in density within the flow. This results in a lower overall turbulent kinetic energy and noise emission due to turbulent mixing in hot jets compared to cold. However this doesn't necessarily correspond to lower overall noise emission. For a constant Mach number, a decrease in the turbulent kinetic energy leads to an increase in jet velocity. The noise generated by the increased jet velocity is greater than the reduction of noise due to the lower turbulent kinetic energy. From this it is clear that the effect of temperature on the emission of noise cannot be explained in a general statement.

In order to better describe and predict turbulent mixing noise, you must also understand and be capable of predicting the large scale structures because they are the primary contributor to mixing noise. This is accomplished through the Stochastic Wave Model. This

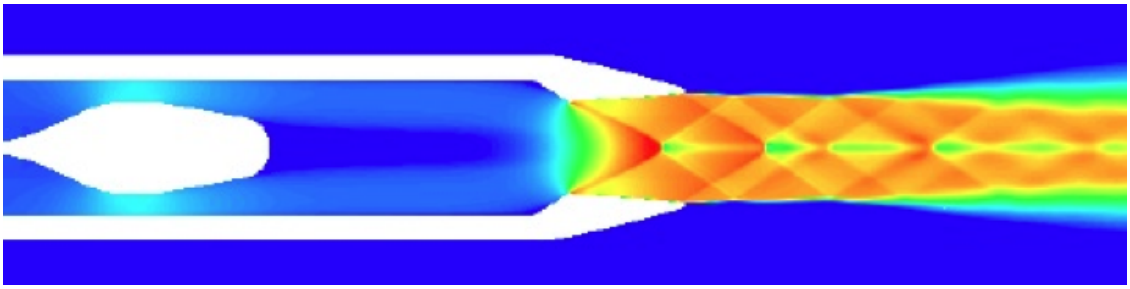

Figure 2.4: Supersonic Shock Structure Calculated Using LES[3]

model draws from known characteristics of supersonic jets to provide a statistical prediction method. It is based on the fact that the rate of growth within supersonic jets in the stream-wise direction is very small. This allows for the assumption that the flow, more specifically the turbulence statistics, change very slowly as it moves downstream. From this it can be assumed that the flow is in a state of quasi-equilibrium and through the use of statistical mechanics, the turbulent structures can be represented by a linear wave. This finding verifies the assumption made above regarding the generation of sound through turbulent mixing.[2]

2.4.2 Broadband-Shock Noise

When explaining broadband-shock noise the shock cell structure must first be introduced. In the case of most supersonic jets, ideal expansion is not achieved. As a result there exist oblique shock or expansion fans, depending on whether the nozzle is overexpanded or underexpanded, which originate from the nozzle tip and propagate downstream. These shock reflect repeatedly downstream until they dissipate, but these also act as a boundary for disturbances within the flow, referred to as the shock cell structure, containing them within the jet wall.[2] Figure 2.4 illustrates the shock cell structure within an overexpanded jet nozzle.

The generation of broadband-shock noise is due to the interaction of these shock cell structures, defined by the reflected shocks withing the flow, with the large scale turbulent structures propagating downstream. As these large structures move through the turbulent jet, they encounter these disturbances contained within the shock cell. As the large structure

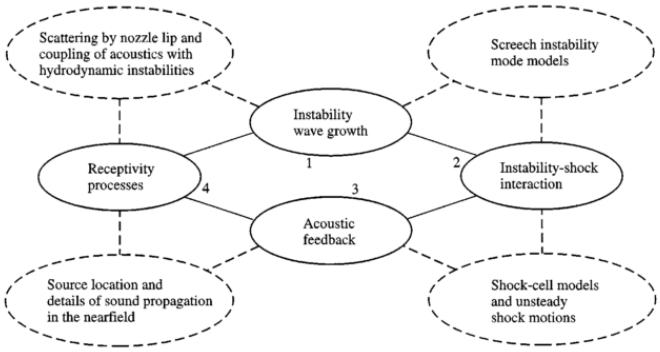

Figure 2.5: Feedback loop for the generation of screech tones[4]

passes through these disturbances it causes a constructive scattering of the structure that generates noise.[2] The noise is considered broadband in nature and rises to a peak through a range of frequencies before decreasing at higher frequencies.[19] The Stochastic Model discussed previously can also be used in the prediction of broadband-shock noise.

2.4.3 Screech Noise

Screech noise, or screech tones, are the least understood of the three sound generation methods for supersonic jets and was first studied by Powell[20] in 1953. While this phenomenon has been observed experimentally for quite a while, there still exists no method for predicting the intensity of screech tones.[21] This is due to their acute sensitivity to environmental changes around them. They are caused by impinging acoustic disturbances on the mixing layer very near the nozzle exit and are excited due to the presence of Kelvin-Helmoltz instabilities within the flow. These instabilities continue to travel downstream increasing in strength due to their interaction with the mean flow. At some point the instability reaches an amplitude high enough to interact with the shock cell structure discussed previously. This interaction emits an acoustic signal that radiates primarily upstream. This feedback loop was described by Raman[4] in a flow chart shown in Figure 2.5. From this schematic the four mechanisms for the generation of screech tones described above are clearly indicated. Also depicted by the dotted lines are various methods used to simulate and model these various components of the feedback loop. The interaction of the instability waves with the shock-cell

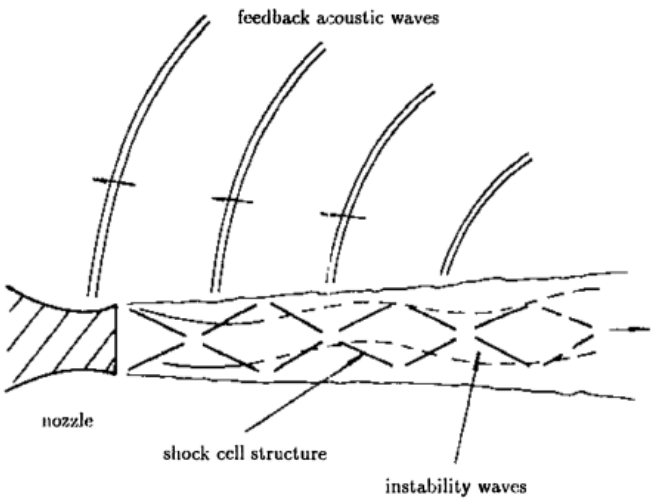

Figure 2.6: Mechanism for the Generation of Screech Tones[2]

structure and the production of the acoustic feedback waves are depicted below in Figure 2.6. The intensities of these screech tone are dependent on a number of variables including Mach number, jet temperature, thickness of nozzle lip, and reflected acoustic wave in the vicinity of the nozzle. The screech phenomenon is the loudest of the three source, producing extreme noise levels capable of damaging equipment on supersonic aircraft. However it is also the easiest to prevent due to its sensitivity to the environment. Simply by varying the nozzle geometry or the jet's exit velocity, this mechanism can be eliminated.

Chapter 3

Review of High-Speed Measurement Techniques

In order to convey the uniqueness of work describe in the following chapters, a broader understanding of high-speed diagnostics employed by experimentalists must be presented. There are numerous high-speed measurement techniques spanning various dimensions of measurement from a single point, to 2 dimensional planar techniques. Multiple methods for each of these measurement areas exist and will be discussed below. Before examining these various methods however, a description of what 'high-speed' measurements are and why they are necessary is required.

To understand the need for high-repetition rate techniques, an explanation of the length and time scales within a turbulent flow is needed. Within a turbulent flow, the large scale structures of a flow are described by the their characteristic length, l and characteristic velocity, u. Using these values, the characteristic frequency, $f_{large} = u/l$, of the large scale motions can be calculated. By simply testing out various values for the characteristic velocity and length, it quickly becomes apparent that in the case of supersonic flows, values of f_{large} can easily range from $10^4 - 10^6$ Hz.[22] From this simple examination of the scales present within supersonic flows, it can be asserted that diagnostic techniques with repetition rates within the range of $10^4 - 10^6$ Hz are needed in order to adequately describe the flow.

3.1 Point Measurements

Point measurement techniques are those most basic methods for gathering data at high speeds for a single location within a flow field. A wide array of methods exist and to discuss all of these is beyond the scope of this thesis. Instead an overview of only a couple of these methods, hot-wire anemometry and laser Doppler velocimetry (LDV) will be presented.

3.1.1 Hot-wire Anemometry

Hot-wire anemeometry is the only high-speed diagnostic technique that will be presented that is not optical in nature. Hot-wire anemometry is based off the principal that the electrical resistance within a metal wire is dependent on its temperature. This principal is utilized for flow measurements by placing a very small heated wire with known properties into a flow. The fluid flow and its fluctuations impart temperature changes on the wire, whose electrical resistance in turn is affected. By measuring the change in the current through the wire, or its temperature, it is possible to determine the flows velocity and its fluctuations. Based off of this relationship, two common hot-wire anemometers are used, constant temperature anemometers (CTA), and constant current anemometers (CCA).[23]

Hot-wire anemometry was first implemented in 1929 by Dryden and Kuethe to measure the fluctuations of subsonic incompressible flow using a CCA. Since this time advances in technology and methodology have allowed for the implementation of hot-wire anemometry in a wide range of flow regimes ranging from subsonic to hypersonic flows. The spatial resolution of a hot-wire anemometer is dictated by the size of the wire being used as well as the scale smallest turbulent structures present within the flow field. If the length of the wire is greater than the scale of the smallest structures, errors are introduced into the measurements. While hot-wire anemometry are capable of measuring fluctuations in high speed flows, it is not without its limitations. One main limitation is its inability to instantaneously gather data over a large flow area. Another problem associated with hot-wires is that the probe must be placed within the flow, and therefore is intrusive in nature. When small scale structures, the probe itself influences the characteristics of the flow field. The final limitation presented pertains to the large difficulties associated with measuring heated, or reacting flows, such as down stream of a heated supersonic jet.[24] Due to these limitations, other methods for high-speed flow diagnostics are required.

3.1.2 Laser Doppler Velocimetry

Another point-wise velocity measurement technique employed by experimentalists is laser Doppler velocimetry (LDV), also known as laser Doppler anemometry (LDA). This is an optical technique that commonly utilizes two lasers beams, or incident light, of known frequencies focused to the same point. The intersection point of the incident beams is the point of measurement within a flow containing small seed particles. These two lasers illuminate the suspended particles in the flow, resulting in a small amount of scattered light. This scattered light can then be measured by a photodetector capable of measuring the frequency of the scattered light. By calculating the frequency difference between the incident and scattered light, or Doppler shift, the velocity can be measured. The velocity is related to the Doppler shift if frequency through the Doppler equation. This method, while more difficult to setup than hot-wire anemometry, has the benefit of being non-intrusive, with the exception of the particle seeding. However, while this method does allow for extremely high-repetition measurements, like hot-wire anemometry, its lack of spatial resolution often necessitates alternative methods for flow measurement.

3.2 Two Dimensional Techniques

Two dimensional high-speed optical measurement techniques are some of the most common methods used today in experimental fluid dynamics. A number of methods fall under this category which include time-resolved particle image velocimetry (PIV), planar laser induced flourescence (PLIF), and planar Doppler velocimetry (PDV). Each of these techniques have their own benefits and limitations which will be discussed below.

3.2.1 Time-Resolved Particle Image Velocimetry

PIV is possibly the most common of all methods discussed above. It necessitates a high-speed laser and camera which captures two correlated images in order to measure the displacement of particles suspended within a flow over a very short time. By cross-correlating

the two images it is possible to calculate the full velocity field imaged by the camera. Most cameras implemented in a PIV setup consist of one camera containing a single interline CCD. This type of camera is capable of capturing only a single pair of time-correlated images which yields a single velocity field. While this method for standard PIV is widely used in experimental fluids, it is incapable of measuring acceleration. For this, three or more time-correlated images are required, resulting in two or more correlated velocity fields. The calculation of acceleration fields is desirable because of its strong relation to the pressure fluctuations in the imaged region. These pressure fluctuations are of considerable interest in fields such as aeroacoustics. While time-resolved PIV yields more valuable data than standard PIV, it is considerably more difficult, requiring a high-speed camera capable of gathering a number of correlated images as well as a high-speed laser that can produce high repetition rate laser pulses. This was accomplished by Wernet and Oplaski[25] to study a Mach 1.3 jet using a a pulse burst laser system operating at 500 kHz and a camera capable of capturing eight frames at a MHz rate. The Cooke Corp. HSFC-Pro camera had 1280 $\times$ 1024 resolution containing 4 separate interline CCDs each with a different optical path. The separate optical paths presented problems due to their slight misalignment reducing their accuracy to approximately 0.25 pixels.[22]

Murphy and Adrian[26] in 2010 utilized the same camera systems to study the blast waves generated by an explosive detonation. Rather than using a pulse burst laser, a series of four Quantel USA double pulse laser systems were combined to produce an eight pulse laser chain. Such an arrangement allowed for the tuning of each individual laser pulse to yield a very consistent pulse intensity across each of the eight pulses.[22] The experiment yielded good results in which the time evolution of blast wave was measured. Some of the problems encountered during the experiment relate to difficulties maintaining adequate particle seeding, particle lag, and the small movement of the shock wave from one frame to the next.

3.2.2 Planar Laser Induced Fluorescence

PLIF is a flow visualization and quantitative measurement technique that utilizes the physics regarding the energy state of the molecules of certain gases. In certain species of gases, if its electrons are excited to a higher energy state, these molecules fluoresce, emitting photons as the gas returns to its original energy state. In order to excite the particles, a tunable wavelength laser is required. This fluorescence of the particles is then captured using a detector, which today is most commonly a camera. The intensity of the fluorescence is directly related to the number of molecules within the volume.[27] The various species that are commonly used in PLIF are OH, NO, Na, 02, CH, CO and acetone. It is often used in combustion diagnostics and reacting flows because of the presence of these molecules. One technique developed by Kaminski et al[28] to study a turbulent nonpremixed methane-air flame utilized four Nd:YAG lasers to pump a single dye laser. This allowed for the capturing sequences of eight images at up to 8 kHz. However this process was limited by the intensity needed to pump the dye laser.

Today, high speed PLIF systems utilize an optical parametric oscillator which allows for almost instantaneous excitation and emission of photons on a nsec scale.[22] This was developed by Sjoholm et al.[29] in 2009 where an energy output per pulse of the OPO system was measured down to 400 nsec. In 2008, Jiang and Lempert[30] were able to conduct NO PLIF at repetition rates as high as 250 kHz. A similar test was conducted in NASA-Langley's 31" Mach 10 wind tunnel by Jiang et al[31] where NO PLIF was used to achieve repetition rates as high as 1 MHz. Approximately 200 sequences of time correlated images consisting of between 10-20 frames each were gathered over a flat plate model.

3.2.3 Planar Doppler Velocimetry

Another optical method for measuring high-speed flows is filtered Rayleigh scattering. This method utilizes the Doppler shift in frequency experienced by scattered light. This frequency shift is a function of the particles velocity as well as the optical geometry. This

shift however is small in magnitude and is difficult to measure. This is addressed by imaging through one of several gases that have distinct transmission and absorption on a similar bandwidth. By imaging the transmission and absorption of light traveling through a glass cell containing one of these gases placed in front of the camera lens, the frequency of Doppler shift can be determined.[22] This method yields enhanced flow visualization images capable of acquiring data in flows with Mach numbers in excess of 2. While useful, filtered Rayleigh scattering gives only qualitative and very basic quantitative data.

This shortcoming of filtered Rayleigh scattering was addressed by Thurow et al.[32] in 2005 with the developement of a MHz rate planar Doppler velocimetry (PDV) technique. This approach a yields one velocity component of the entire flow field by utilizing both a filtered signal image and an unfiltered reference image both gathered simultaneously. By using the ratio of these two images to calculate the local Doppler shift of the scattered light, and then drawing on the relationship between frequency shift and velocity found in the Doppler shift equation, the magnitude of the velocity component can be determined. [22] This technique was demonstrated on a supersonic jet where a high contrast of the velocity field could be seen between the jet core and ambient air. Detailed features of the mixing layer were also visible, indicating the significant velocity gradients within the mixing layer.[22]

3.3 Experimental Aeroacoustics

High-speed diagnostic techniques are commonly used in experimental aeroacoustics. Some of these techniques are similar to those described with the inclusion of other techniques such as microphone arrays. A large portion of aeroacoustic research has been aimed at the localization of sound sources within a turbulent jet due to various mechanisms. This work started in the 1970s and is still the focus of a significant experimental efforts today. Early experimental techniques developed by Laufer et al.[33] using a directional microphone system, also referred to as an acoustic mirror. The technique for identifying the location of noise sources by cross-correlating series of microphones was developed by Billingsley and

Kinns[34]. This method allowed for the estimation of time varying sound distribution and laid the foundation for future sound source localization via cross-correlation which is still employed today. Since these early efforts, numerous techniques have been developed often designed for examining the specific mechanisms of noise generation, turbulent mixing, broadband shock, and screech noises, which were describe above. Some of these experimental techniques and their findings are presented below.

3.3.1 Turbulent Mixing Noise

Turbulent mixing noise, as previously stated, is related to the generation and collapse of large and small scale structures within the jet flow. This topic has been widely studied through experimental means, some of which are presented here. Humphreys et al.[35] and Narayanan et al.[36], through a joint study found that the largest source within the noise distribution is located at the collapse of the potential core. This study was conducted on a cold and heated subsonic turbulent jet using a linear phased microphone array. An extension of this work was conducted by Hileman et al.[37] on an ideally expanded high speed jets using a 4 microphone inline array. Flow visualization data was taken simultaneously using a pulse burst laser system used in conjunction with a high speed camera from which three mechanisms for sound generation were identified. These consisted of cross-mixing layer interaction, tearing of large turbulent structures, and the rollup of large turbulent structures. It was found that during periods of high amplitude sound production, a larger quantity of ambient air was entrained by jets large turbulent structures, which corresponded to mixing layer extending further into the jet core.

A method for locating individual acoustic sources in a high-speed, high Reynolds Number, turbulent jet using a 3-D microphone array was also developed by Hileman et al.[38] This technique replaced the linear array used in his previous work with a 3-D array capable of locating sound sources in three dimensions. It was found that this technique was capable of locating noise sources from a plasma arc, a high-frequency fluidic device, as well as the

radial distribution of acoustic sources in a high speed jet. This technique was later applied by Hileman et al.[39] in conjunction with flow visualization using a high speed camera and a pulse burst laser system to study the evolution of large-scale turbulent structures in a Mach 1.28 jet. This method allowed for the comparison of acoustic data to the time evolution of the jet flow field. It was found that the generation of sound coincided to the formation of large scale structures, leading to greater entertainment of air, eventually resulting in the collapse of the structure and noise generation. It was also established that similarities exist between low-speed and high speed jets in relation to their mechanisms for sound generation.

The localization of sound sources was also studied by Papamoschou and Dadvar[40] on a cold Mach .9 jet using a small-aperature microphone phased array. Using a beamforming technique initially developed by Venkatesh et al.[41] it was found that the noise emanating 30° from the jet axis was due to large-scale turbulence, while noise emanating 90° from the jet axis was attributed to fine-scale turbulence. Both of these noise sources were found to peak in amplitude near the end of the potential core and the location of the noise source moves closer to the nozzle exit as frequency increases.

A recent study conducted in 2011 by Baars et. al.[42] examined effect of heat on turblent mixing noise in an ideally expanded, heated Mach 1.553 jet. Because the flow was ideally expanded, no shocks exist in the jet's flow, thus eliminating the source of both broadband shock noise and screech tones. A linear array of 10 microphones were utilized to capture the acoustic near-field pressure signatures just downstream of the collapse of the potential core. A far-field array consisting of 12 microphones spanning $20^\circ - 150^\circ$ from the jet axis was used to capture the far-field acoustic data. It was found that the mechanism in which mach waves, or sound waves, radiate from the source is dependent on numerous flow conditions such as refraction, growth and decay of Mach angles, dispersion and nonlinear propagation.[42] It was also shown that near-field and far-field pressure regions are linearly coupled. However a number of questions remained unanswered regarding the varying acoustic arrival times between hot and cold jets.

3.3.2 Broadband Shock Noise

Broadband shock noise is the most widely understood source of supersonic jet noise within the field of aeroacoustics. Despite this, shock associated noise remains a topic that is widely studied around the world. Norum and Seiner[43] in 1982 investigated the source of broadband shock noise using near-field and far-field acoustic measurements on unheated convergent and convergent-divergent nozzles. They found in the convergent case that the peak Helmholtz number of broadband shock noise was independent of the nozzle pressure ratio if it was based on the ambient speed of sound and the length of the shock cells. It was also found that the shock associated noise acts primarily in the upstream direction, except in the case of high pressure ratios where it acts omnidirectionally. The near-field data taken for highly underexpanded convergent nozzles also pointed to the fact that a small region of the shock cell system is the dominant contributor to the broadband shock noise.Tam[44] in 1982 developed a stochastic model theory for broadband shock noise which was capable of predicting the near-field and far-field pressure spectra associated with the shock noise. These results were found to have good agreement with experimental data taken at the time.

More recent examinations of broadband shock noise have utilized advances in measurement technologies, particularly within the realm of particle image velocimetry (PIV). Bridges and Wernet[24] at NASA Glenn developed a time-resolved PIV (TRPIV) technique to examine a Mach 1.05, 1.185 and 1.4 jet at various temperatures for both ideally expanded and convergent nozzles. This method was capable of gathering 4 GB of image data at a primary sample rate of 10 kHz. A sample rate of 25 kHz was achieved at a smaller field of view. The system was arranged using two identical cameras with a field of view spanning 6 jet diameters gathering data simultaneously at varying positions downstream. The total imaged area spanned from 1-20 jet diameters downstream of the nozzle exit. It was found that when fully expanded, the effect of heat on the turbulence within the flow can be accounted for by considering the momentum change due to the flow's decreased density. However, for non-ideal cases when shocks are present, it was found that the temperature had little effect

on the shock structure. It was also determined that in the presence of screech tones, the density factor was dominated by the shock noise regarding their role in turbulent velocity and mixing.

3.3.3 Screech Noise

The generation of screech noise caused by the irregular expansion of supersonic flow through a jet nozzle is the least understood sound source and has been the focus of a large experimental effort since it was first observed by Powell in the early 1950s. Due to Powells inability to obtain high-quality microphones, his early experiments utilized a schlieren system only in which he observed sound waves propagating upstream. This work was continued by Poldervaart et. al.[45, 46] in the late 60s and early 70s using a flow visualization technique that captured the feedback loop of screeching jets. More recent experiments conducted by NASA as described in Raman[4] have been aimed at identifying the various screech modes within supersonic jet. Experimental attempts to predict screech frequencies have also been made, notably by Tam[47] in 1986 where he stated that screech noise is a special case of broadband shock noise. He also presented theoretical calculations for frequencies associated screech tones which agreed with experimental findings. These findings however are limited to rectangular nozzles and require that the unsteady shock-cell structure of the jet is known.[4]

Screech noise emanating from an underexpanded Mach 1.19 and 1.49 jet was examined by Panda[48] using phase-averaged microphone measurements and Spark schlieren visualization. At different phases of the screech cycle, large organized vorticies were observed interacting with the shock train present in a supersonic jet. It was also shown that the primary length scale governing the generation of screech noise is directly related to the interference pattern caused by hydrodynamic and acoustic fluctuations. This new length scale was coined 'standing wavelength' and allowed for an exact expression of the screech frequency. It was also observed in a similar study by Panda[49] using Rayleigh scattering and phase-averaged microphones that Kelvin-Helmholtz instability waves emanating from

the nozzle generate organized eddies that then interact with shock cells to produce noise. These instability waves will periodically modulate across the jet shear layer, at which these location experience a local maximum in convective velocity and an antinode in the near-field pressure fluctuations. This all leads to the generation of screech tones, which can now be attributed to modulation of the instability waves.

In 2011 Andreét al.[50] reported on a new shock tracking procedure used for observing screech noise. This method employed a Z-type schlieren system and two near-field pressure sensors to gather data. By processing the data through pattern matching algorithms, Andre observed that:

1. "The oscillation frequency of shocks is equal to that of screech."
2. The mode of oscillation of shocks, symmetric or antisymmetric, is the same as the screech mode.
3. The motion magnitude is an increasing function of the screech amplitude."
4. The relation between screech amplitude and shock oscillation magnitude is peculiar to each screech mode."[51]

Chapter 4

Experimental Arrangement

4.1 Anechoic Jet Lab

The experiments were conducted at the National Center for Physical Acoustics' (NCPA) Anechoic Jet Laboratory (AJL) located at the University of Mississippi. The AJL is a 19-by-20-by-8 ft anechoic chamber built specifically for the study of high speed, high temperature jet noise. Fixed fiberglass wedges used for sound absorption cover two sides of the chamber as well as its ceiling. Both the upstream and downstream walls contain openings to allow ambient air to be pulled through the room so that an even temperature can be maintained during testing. In order to maintain ease of access to the rooms equipment, the floor consists of a solid concrete slab that is covered during testing using fiberglass wedges fixed to rolling dollies. [3] This setup can be seen in Figure 4.1.

The jet rig visible in Figure 4.1a and shown specifically in Figure 4.1b is supplied air from an 1100 hp Ingersoll-Rand Centac compressor through a desiccant dryer system. A maximum volumetric flow rate of 5000 SCFM of dry ($-40°$) air at 125 psia enables continuous operation of the facility at desired test conditions. Control valves operated in a closed-loop

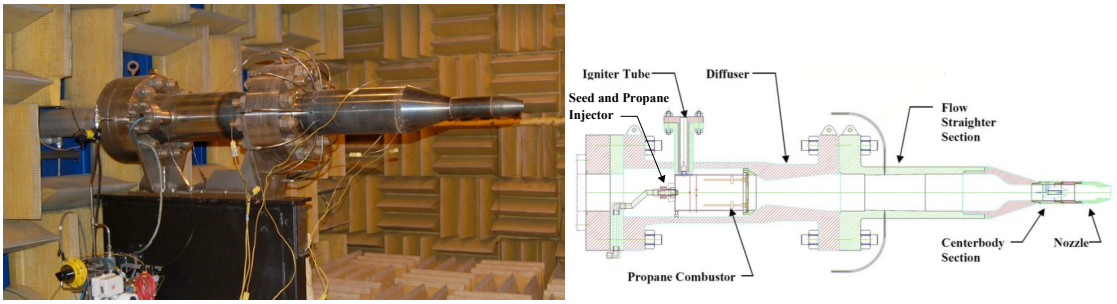

(a) Nozzle Assembly (b) Nozzle Schematic[3]

Figure 4.1: Anechoic Jet Lab

system allow the exit Mach number to be maintained within 1% of a specified value. Heat can be added to the flow through the use of a gaseous propane burner system as shown in Figure 4.1b. The propane combustor is housed well upstream of the nozzle assembly and is followed by a ceramic flow straightener and settling chamber. Although multiple nozzle assemblies exist for this system, only the configuration shown in the schematic that includes the centerbody section was utilized for the work in this paper.

4.2 Pulse Burst Laser System

A pulse burst laser system designed and built at Auburn University was used for illumination in the PIV setup. It has been shown in previous publications that the system is capable of delivering high energy 532 wavelength pulses at MHz rates.[52, 53] The laser design in its current state has undergone a number of improvements. These include a new JDSU NPRO 126 continuous-wave Nd:YAG seed laser as well as an additional three flash lamp amplification stages. These improvements have made for a more consistent system capable of producing energies in excess of 50 millijoules per pulse for use in both PIV as well as flow visualization. A schematic of the current laser system is shown below in Figure 4.2. The laser was operated at two hertz, with each burst containing 65 pulses with $1\mu s$ between each pulse.

The pulse burst laser operates in what can be considered three separate stages: pulse generation, pulse energy amplification, and frequency conversion, which are labeled in Figure 4.2. The pulse generation stage is responsible for the slicing of the 1064 nm continuous wavelength (CW) laser into very small individual pulses which is done by passing the CW laser through an acoustic optic modulator (AOM). The AOM contains a small optical crystal and a piezoelectric transducer. The transducer, triggered by a control box and timing system, produces acoustic waves inside the optical crystal causing its index of refraction to change. This change in the index of refraction deflects the incoming laser so that it continues into

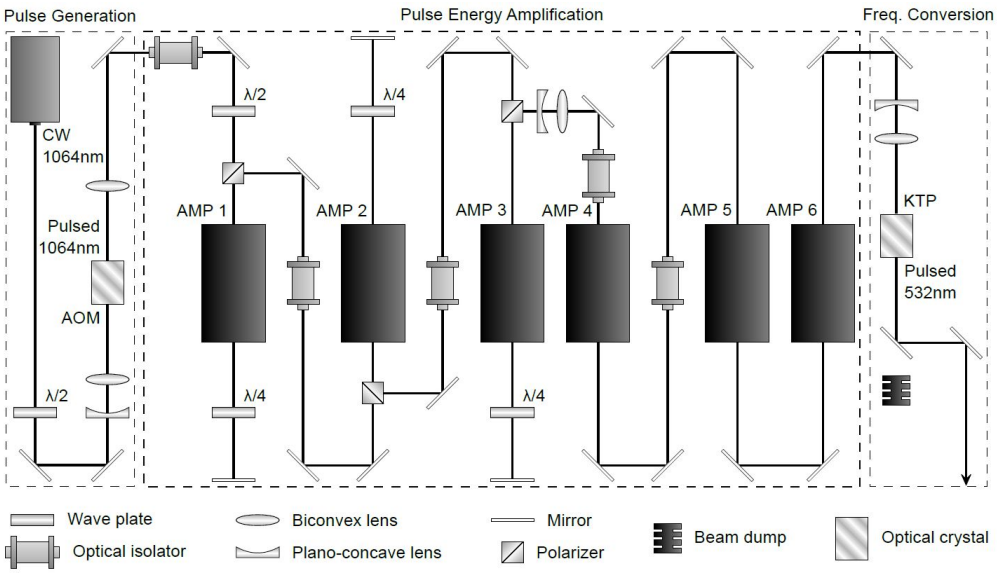

Figure 4.2: Pulse Burst Laser System[5]

the remaining two stages of the pulse burst laser. By controlling the rate at which the piezo-electric transducer produces acoustic waves, the number of short duration pulses produced can be adjusted.

The laser pulses diffracted by the AOM then enter the pulse energy amplification stage. This stage consists of six Nd:YAG flashlamp-pumped amplifiers of increasing diameter and voltage. The first three flashlamps are arranged in a double-pass configuration and is achieved through the implementaion of waveplates and polarizers. The remaining three amplifiers consist of a single-pass configuration. At the conclusion of the amplification stage, the laser pulses have increased by a range of $10^7 - 10^8$ in energy. [54]

The final stage of the pulse burst laser system pertains to the conversion of the lasers wavelength to 532 nm from the original 1064 nm. This conversion is necessary to convert the laser into the visible spectrum of light, where 532 nm is green light typically used in PIV systems. This is done through the implementation of a KTP crystal which converts the laser in a nonlinear process which leads to significant, yet necessary losses in energy levels. Through the use of various lens configurations, the laser pulses are then collimated so that it may travel the required distance to the experimental area. There the laser is manipulated,

often into sheets or volumes of light depending on the experiment. In the case of a PIV experiment, a cylindrical lens is used to shape the circular laser beam into a thin sheet of laser light.

4.3 Cordin 222-4 Camera

In order to acquire images at the desired MHz frame rate, a Cordin 222-4G gated intensified CCD framing camera was used. It is capable of acquiring 16 images at frame rates up to 2,500,000 frames per second, or 8 frames at 4,000,000 per second. The camera contains eight Kodak KAI-4022 CCD sensors with 2048×2048 pixel resolution. The actual resolution was reduced due to the intensified effects of the microchannel plate (MCP), which intensifies incoming light but decreases the effective resolution. The MCP is necessary because the Cordin contains 8 independent CCD channels, each coupled to their own MCP. All incoming light is beam split 8 ways into each of these channels. While this allows for very high frame rates, it necessitates light intensification in order to maintain adequate illumination. Just as important as the amplification, the intensifiers also provide gating of the signal so that the exposure of each CCD is controlled by the MCP's allowing for very short exposure times. Because the CCD described above is an interline CCD, each channel can acquire 2 frames at a minimum time spacing of just $3.2\mu s$, giving 16 total images per sequence. An interior and exterior view of the Cordin camera can be seen in Figure 4.3, which illustrates the multichannel setup that the camera utilizes. Both frames in each of the 8 channels can be independently controlled giving the ability to customize the temporal spacing to their specific needs. Additionally, the ability to obtain several particle images at varying time intervals relative to one another has provided the means of performing HDR PIV. Such measurements offer significant improvements over conventional PIV results since optimum temporal separations can be selected for different particle locations depending on the local velocity.

(a) Exterior View (b) Interior View

Figure 4.3: Cordin 222-4G High-Speed Camera[6]

4.4 Experimental Setup

For this experiment a conic, converging-diverging nozzle was operated at the over expanded condition The nozzle had an exit diameter of two inches with a throat to exit area ratio equivalent to a design Mach number of 1.74. The operational conditions for the experiments were maintained at Mach 1.56 and a total temperature of $1350°F$ for all the data collected. As stated in the previous section, the Cordin camera gathers 16 images per sequence and was operated at a rate of 1 MHz. This would provided a total temporal spacing of $15\mu s$. However due to technical difficulties with the camera, only 14 images were gathered per sequence with a temporal span of $13\mu s$. A complete list of the camera settings as well as the PBL settings can be found in Tables 4.1 and 4.2. The problems that were encountered and the steps taken to overcome them will be discussed in greater detail in the next chapter. The image region was located at x/D of 4.03 to 5.25 jet diameters downstream and at a y location of y/D of .3 to 1.52 diameters below the jet centerline which gives a total field of view of $2.5 \times 2.5\, in^2$. The field of view was chosen so that, at the given axial location, it would span from just beneath the jets centerline into the ambient air, encompassing the entire shear layer. This was based off of experimental data that indicted the growth of the shear layer in the axial direction. However, based on experimental data presented later in the thesis, this placement was too low, resulting in the failure to image the entire shear layer. This setup can be seen below in Figure 4.4 as well as Figure 4.5.

Aluminum oxide particles were used to seed the flow for the PIV measurements. The particles had a nominal diameter of $0.1\mu m$ so as to accurately follow the flow yet withstand

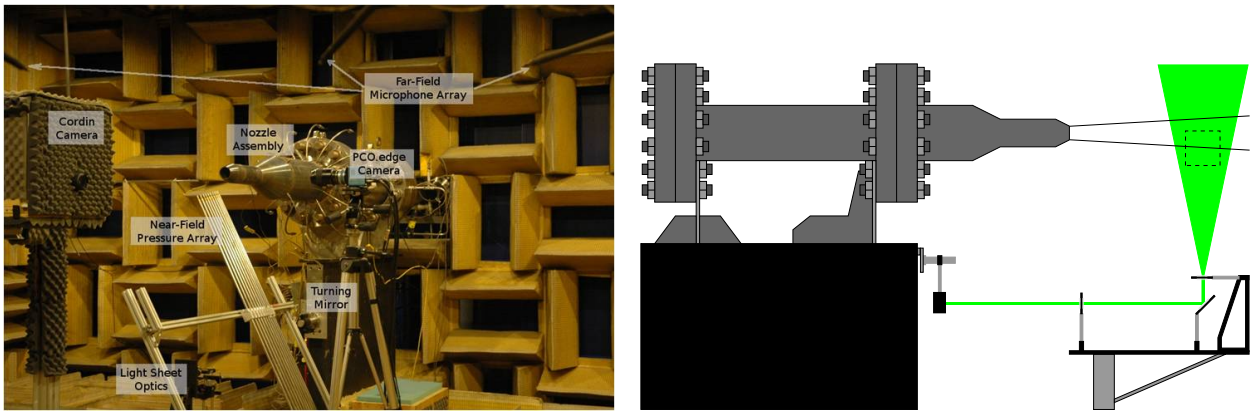

(a) Complete experimental setup (b) Optical arrangement and image region

Figure 4.4: Experimental Arrangement

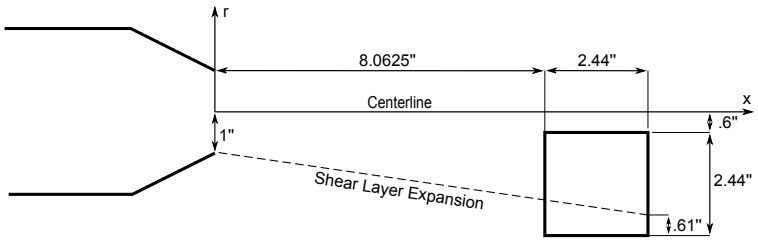

Figure 4.5: Diagram of image region

the high temperatures of the jet.[3] They were injected into the flow upstream of the nozzle exit in an ethanol solution. The ethanol-alumina solution was pressurized in a separate container by nitrogen and forced into the burner assembly where the ethanol burned leaving the particles suspended in the flow. This method provides an even particle distribution throughout the flow while delivering adequate seeding for the PIV experiments.[55] The camera and laser system was synchronized to operate simultaneously with an array of near and far-field microphones. A PCO edge camera was also set up to simultaneously take streak images of the flow, where one image was exposed to all 65 of the laser pulses. While this data was an integral part of the entire experiment, the focus of this paper is on the time-resolved PIV data and a more in depth description of these systems is not included for this reason. The four measurement systems were all triggered through an system of timing boxes. A Stanford timing box controlled the master trigger that activated the entire system. This timing box sent two triggers, one to the PBL Quantum Composer timing box, and the other

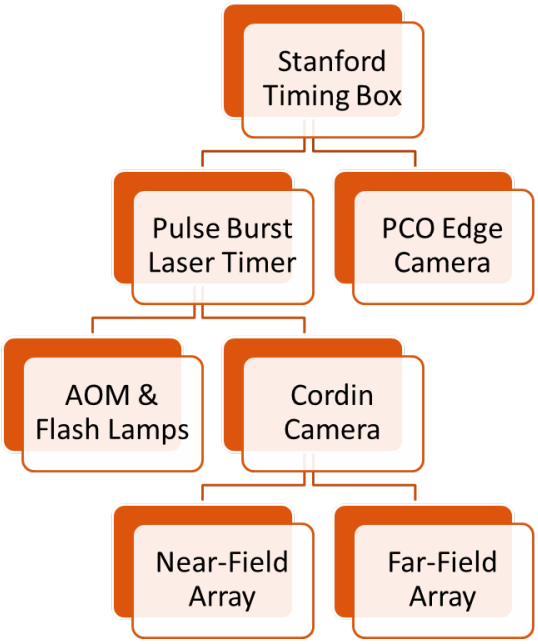

Figure 4.6: Flow chart of triggering mechanism for the various measurements systems used.

to the PCO camera which was synced to the laser pulses of the PBL. The PBL timing box in turn triggered the AOM and the flash lamps on the laser table as well as the Cordin Camera, which was also synced to the pulses of the PBL. An output signal from the Cordin camera was used to trigger the near and far-field microphone arrays, which utilized a circular buffer to ensure pressure measurements were taken prior to and immediately following the received trigger. A flow chart depicting this triggering mechanism for system is shown in Figure 4.6.

4.4.1 Experimental Timing

Shown in Table 4.1 are the individual camera settings for the Cordin during the data acquisition. The constant "A" for the frame timing consisted of a 29μs delay while the constant "B" was set to a delay of 549μs. The individual MCP gain offsets for each of the eight cameras are also shown. The global MCP gain was set at 60 and the global CCD gain was set to 90.

Camera	Frame 1-8 (μs)	Frame 9-16 (μs)	Gain Settings
1	A + B + 1	A + B + 7	+ 23
2	A + B + 2	A + B + 8	+ 8
3	A + B + 0	A + B + 13	+ 7
4	A + B + 3	A + B + 9	+ 10
5	A + B + 4	A + B + 10	+ 18
6	A + B + 5	A + B + 11	+ 15
7	A + B + 6	A + B + 12	+ 9
8	A + B + 0	A + B + 13	+ 2

Table 4.1: Experimental timing and settings for Cordin

Table 4.2 displays the experimental settings used for the PBL system. The constant "A" corresponds to the same delay listed above. The voltages and timing used implemented by the PBL were chosen to yield the highest possible laser intensity while maintaining an even energy distribution across all 65 of the laser pulses. While only 16 pulses were imaged by the Cordin camera system, a total of 65 pulses was retained because when decreasing this number, it was found that the energy profile of the pulses became unstable.

Amp/Camera	Channel	Voltage	Timing Delay μs
1	A	425	A+70
2	B	475	A+150
3	C	525	A+170
4	D	800	A+130
5	E	1000	A+95
6	F	890	A+190
Camera	G	-	A+549

Table 4.2: Experimental timing and settings for pulse burst laser

4.5 Experimental Speed Bumps

Using the experimental arrangement described above, early attempts at gathering data were made. Problems however quickly arose involving image quality. Certain images from one or more of the eight cameras were at times blurred beyond usability. It was initially believed to be a problem with the focus of the individual cameras within the Cordin system. This however was quickly ruled out because upon closer inspection, the problem was

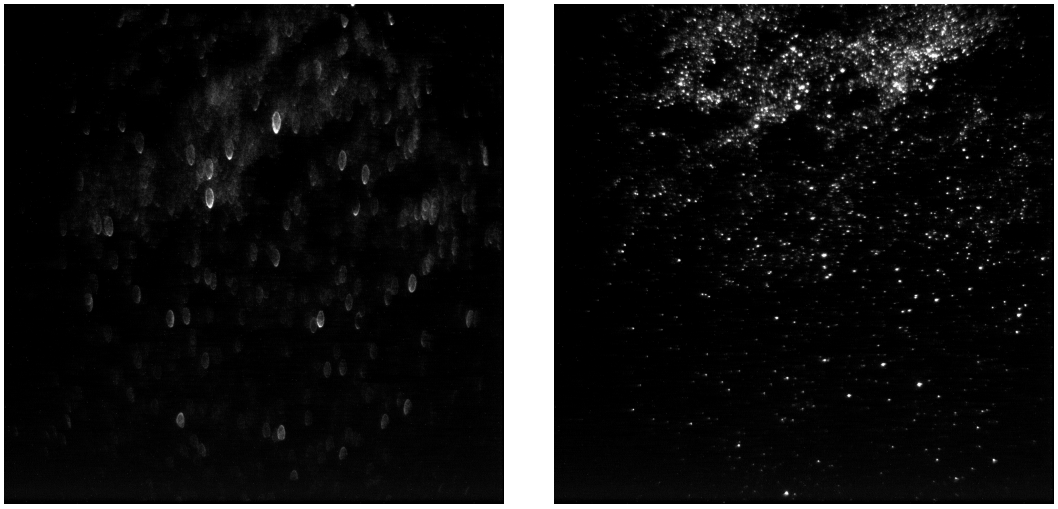

(a) Blurred image due to acoustic vibrations

(b) Focused Image

Figure 4.7: Intermittent image blurring due to acoustics

intermittent across all of the camera frames. A particular camera image would be blurred in one sequence, but in another would contain focused particles. An example of this can be seen in Figure 4.7. The cause of the problem was finally attributed to a design aspect of the Cordin camera. As previously described, the Cordin camera splits incoming light into eight separate optical paths, each leading to an individual image sensor. In order to prevent optical distortions, very thin pellicle beam splitters were used in the camera design. These optical splitters, when exposed to the extreme environment of the AJL, would experience vibrations induced by the high acoustic levels inherent to lab's operation. In order to mitigate the vibrations, an acoustically shielded box was constructed to encase the Cordin. This can be seen in Figure 4.8. The box was constructed using a wood frame paneled on 5 sides using sound attenuating ceiling tiles. Two inch sound absorbing foam was attached to the exterior and interior of the box. Multiple layers of tile and foam were placed on the box's front face due to its close proximity to the noise generating turbulent jet. The sound absorbing materials served a dual purpose of preventing acoustic reflections which could interfere with the near and far field pressure arrays. The acoustic shielding did not eliminate the blurring entirely but did drastically reduced the frequency at which it occurred. However,

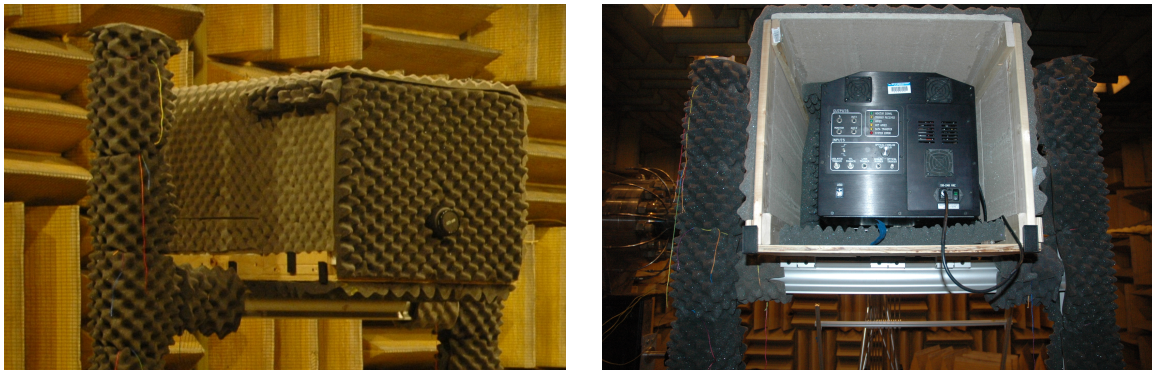

Figure 4.8: Acoustic shielding for the Cordin Camera

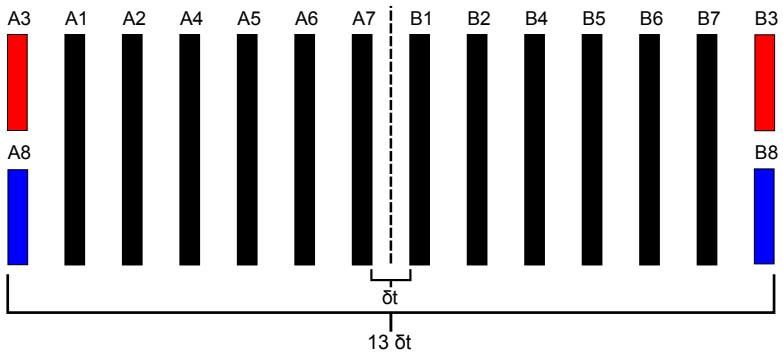

Figure 4.9: Sequence timing to correct for camera problems. ($\delta t = 1\mu s$)

due to the arrangement of the beam splitters, the third camera within the Cordin continued to frequently acquire blurred images.

Another problem encountered in the setup also involved the Cordin camera. As described above, 16 images were to be taken per sequence at 1 MHz. However, shortly before final testing, channel eight cut out, dropping the number of usable images per sequence from sixteen to fourteen. Due to this, as well as the continued blurring of camera three, the sequential timing of each frame was rearranged such that the affected images were taken at the beginning and end of each sequence. This was done so that despite the image quality of either of the affected cameras, a minimum of twelve sequential images could be obtained. An illustration of the described timing configuration can be seen in Figure 4.9. It is important to note that halfway through data acquisition, channel eight began working again, allowing for it or channel three to be used in PIV processing based on image quality.

Despite these setbacks, the experiment was conducted over the course of a week in which 308 time-resolved velocity sequences synchronized with near and far-field microphone readings were gathered. Each velocity sequence consisted of 14 images with a temporal spacing of 1 μs between each frame. The low number of sequences gathered was due to the significant time required (15 sec) by the Cordin camera to download each sequence. This, coupled with the operation costs of the facility as well as the limited amount of particle seeding available led to a lower than desired number of acquired PIV sequences.

Chapter 5

Image Processing

With any PIV experiment, processing steps are taken to convert the experimental particle images into velocity data. In most cases this simply involves the use of PIV software which correlates image pairs to determine velocity vectors. However, due to the complicated nature of the experiment and the equipment used, problems regarding the data quality that arose during the image acquisition. These problems were consistent across all the image sequences gathered during the experiment and fall into six main categories, five of which can be seen in Figure 5.1.

The first image problem was due to poor particle seeding in the lower third of the image indicated by the solid rectangle. This was in-part due to a lower particle number density in this region, but mainly due to the low placement of the camera which led to a significant portion of the field of view being located outside the jet's shear layer in the ambient air. The second issue which is indicated by the dashed rectangles located in the top corners of Figure 5.1 was in part due to low laser intensity near the edges of the field of view. In order to increase the laser intensity within the imaged region, the laser sheet was narrowed to almost exactly fit the field of view. However the edges of the laser sheet contained lower intensity light which negatively affected the data quality within these regions. Vignetting also played a role in decreased particle intensity in the image's corners. This was due to the use of a 200 mm camera lens that was not matched to the internal optics of the Cordin Camera. The use of this lens was unavoidable however because it was the only lens available in which the desired field of view could be achieved while maintaining an adequate standoff distance from the high temperature jet flow.

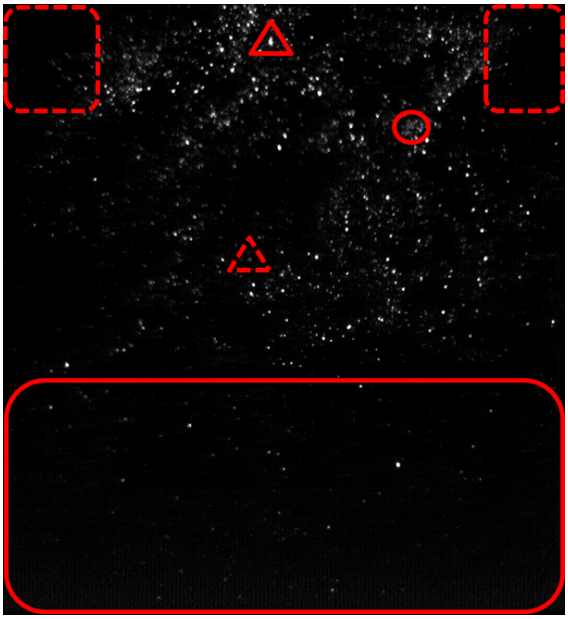

Figure 5.1: Highlighted data quality problems within raw experimental images.
1) Solid Rectangle: Large region of low particle density.
2) Dashed Rectangles: Low laser intensity in the image's corners.
3) Solid Triangle: Large saturated particles.
4) Dashed Triangle: Very small dim particles.
5) Solid Circle: Noisy or hazed particles due to intensified affects of the camera.

The third and fourth data problems indicated by the solid and dashed triangles refer to the presence of both large saturated particles, and small dim particles within the experimental data. This could be caused by a number of problems but is most likely due to inconsistent particle seeding and/or inadequate illumination of the field of view. The fifth, and final problem indicated in Figure 5.1, is marked by the solid circle. These area contains small particles that are hazed, or seemingly blurred together. This was caused by the intensified affects of the Cordin camera system which decreased the overall image resolution and made it difficult to discern between individual particles in regions such as this. The sixth, and possibly the most significant of those encountered, is due to the misalignment of the images within each image sequence. This was caused by the existence of eight separate optical paths within the Cordin camera, each leading to a separate CCD. This misalignment lead to significant jitter, or movement, between the frames of each image sequence.

While each of the problems described above seems minor in terms of their individual impact on data quality, when combined resulted in severe and unacceptable error levels. Therefore to address these problems, a methodology for the processing of the time-resolved PIV data which was developed. This chapter discussed in detail the steps implemented to minimize the impact of the image quality problems on the final results. These steps are shown sequentially as a flow chart in Figure 5.2.

5.1 Raw Image Processing

Prior to performing PIV analysis a number of steps were taken to correct the data for image distortions as well as improving the particle recognition. The first step taken was to eliminate "hot" pixels present on each of the CCD's during the experiments by performing a dark subtraction. A "hot" pixel refers to a pixel that records a signal regardless of its exposer to light. After each experimental run, dark images were taken with the Cordin camera's shutter closed. Every time the camera was turned on for a new data acquisition run, dark images were also taken to account for random hot pixels that might have been present at that time. An average for all the dark images for each specific run was then calculated. The background CCD noise was reduced by subtracting the average dark images from their corresponding experimental images. The application of a three by three median filter to each image was then used to reduce the random background noise inherent to MCPs. This helped to distinguish dim particles within the image while cutting out the some of the background noise. Figure 5.3 contains two images illustrating the effects of the filter. A particular region in both images has been zoomed in on as well as their contrast adjusted so that the effects are more visible. It can be seen that the filtered image in Figure 5.3b contains significantly less background noise compared to the unfiltered image in Figure 5.3a while the overall quality of the particles remained intact.

The next step taken was to eliminate camera jitter, image warping and vignetting. Because each camera has its own optical path, the alignment, while close, was slightly

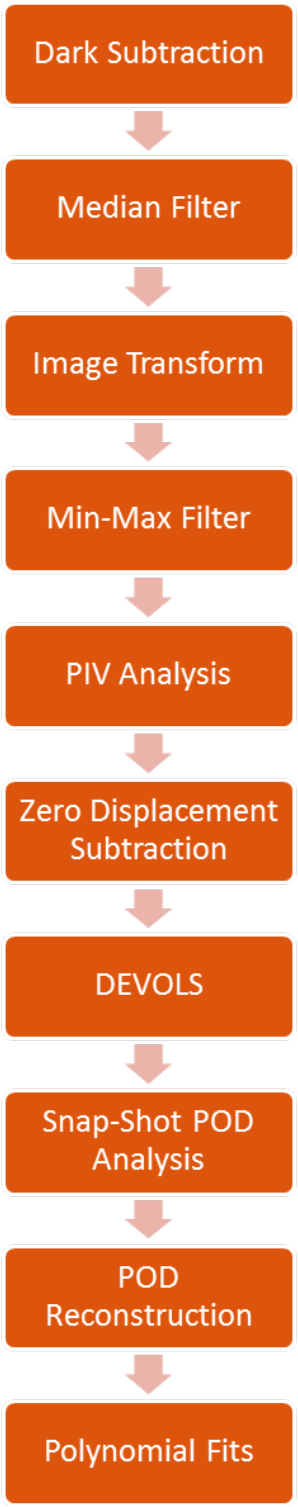

Figure 5.2: Image processing flow chart

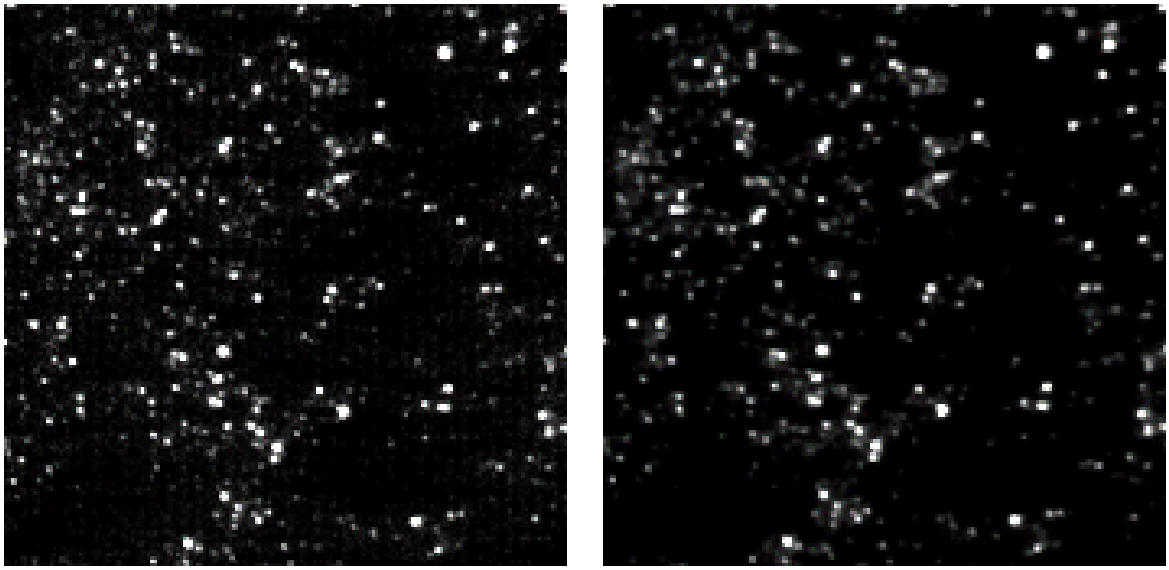

(a) Experimental image prior to filtering (b) Exprimental image after filtering

Figure 5.3: Comparison of raw image data to the 3x3 median filtered image

different. This resulted in jitter, or image movement, between frames, which was present when imaging stationary targets. Also due to the use a lens that was not specifically matched to the internal optics of the camera, vignetting and warping at the edges of the image occurred. This was corrected using a calibration image of a dot card taken prior to and following data acquisition which is shown in Figure 5.4a. The location of each dot's center was determined using a circular Hough transform and is shown in Figure 5.4b. While at first glance these dots may appear to be tightly grouped, by zooming in on one of the groupings, as seen in Figure 5.5, it is clear that significant discrepancies exist in the alignment of the cameras. Errors as large as 10 pixels in the x-direction and 20 pixels in the y-direction are evident. The following steps were implemented to map these dot locations into the tightest possible grouping.

Ideal dot locations were determined by averaging the location at the center of the dot card image across all eight frames, and then placing the remaining "virtual" dots based off of the known dot card pattern. These "virtual" dots represented the ideal location of the dots in the absence of camera jitter, warping, and vignetting. A 2nd order polynomial image transform specific to each of the eight frames was then calculated using the MatLab

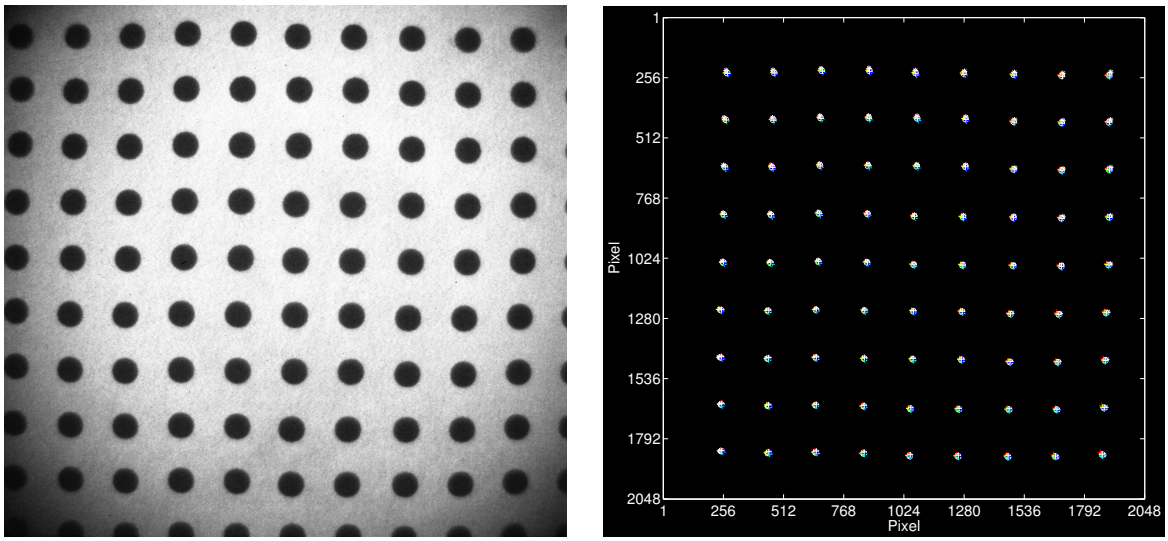

(a) Sample Dot Card Image (b) Dot Locations

Figure 5.4: Calibration Data

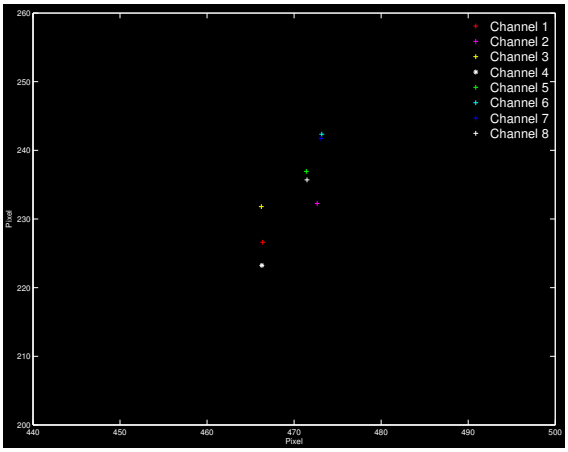

Figure 5.5: Zoomed in location of dots

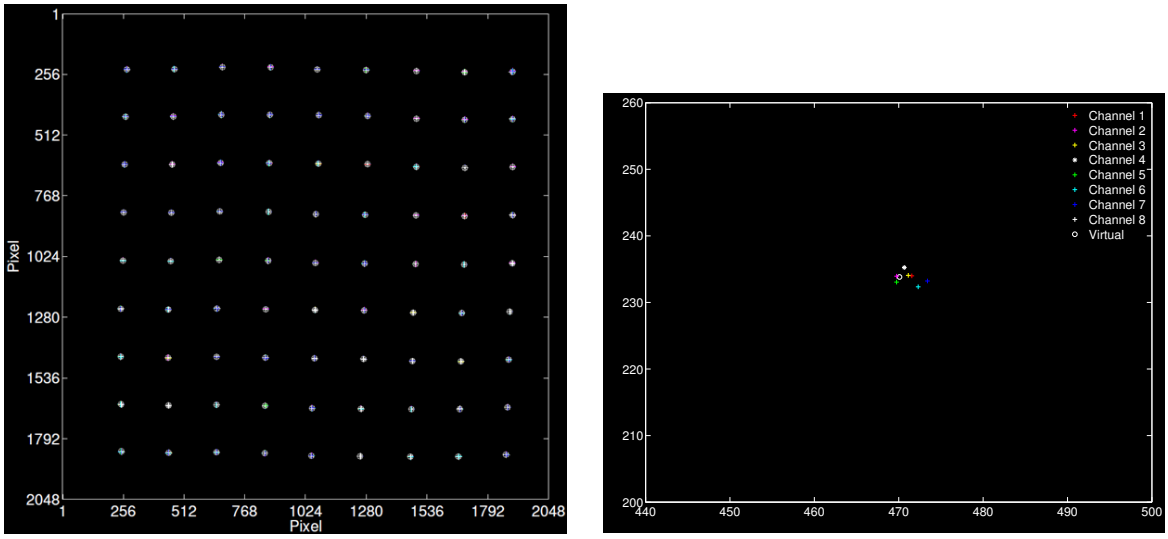

(a) Locations of transformed dots (b) Zoomed in location of transformed dots

Figure 5.6: Effects of Image Transform

function *imtransform* to map each of the original dots found using the Hough transform to the location of the "virtual" dots. Figure 5.6 shows the affect of the transform on the location of the dots. While it can be seen that Figure 5.6a appears to have a much tighter grouping of dots than Figure 5.5, Figure 5.6b clearly shows the improvement. It can be easily seen that these locations are more tightly grouped in the transformed image, showing that frames have been more closely aligned with errors reduced to 2 pixels in both the x and y-direction. These eight transforms were then used on the experimental particle images to correct for the problems listed above.

The final processing step taken prior to PIV analysis was the application of a Min-Max filter to the data in an effort to normalize the particle contrast throughout the images. This is a nonlinear filter that sets the upper and lower bounds of the images intensity within local region, subtracts the lower intensity, and then normalized by dividing by the difference between the upper and lower bounds.[51] The local window size used was nine by nine pixels in size, which enhanced the small dim particles while the intensities of large saturated particles were reduced resulting in smaller, more concise particles. A comparison between an image before and after the application of the min-max filter can be seen in Figure 5.7 where

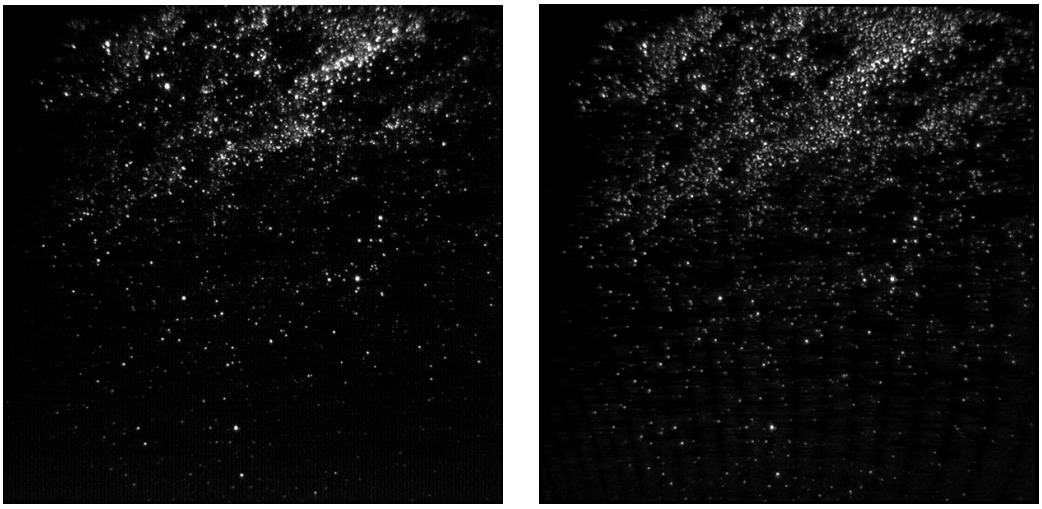

(a) Raw experimental image (b) Image following min-max filtering

Figure 5.7: Effects of Min-Max filter on particle density and intensity

it is clear that the filter helped to enhance the particles within the image region. After the completion of these steps, the data was ready for PIV analysis.

5.2 PIV Processing

Dantec's Dynamic Studio was used to perform the PIV analysis and obtain vector fields for time-resolved PIV as well as HDR PIV for implementation using the DEVOLS algorithm previously discussed.[8] A multi-pass correlation was used with a final interrogation window size of 64x64 and 50% overlap. Three refinement steps were implemented with two initial, three intermediate, and three final passes per per step. Local neighborhood validation was also used and incorporated three iterations with a moving average and a 3x3 neighborhood size. Lastly a central difference method was used to offset the interrogation area. Figure 5.8 shows the ensemble average of all 308 sequences gathered during the experiment, each containing 13 vector fields, which gives a total 4004 vector fields. From this it was discerned what image regions we could expect to contain valid vectors when examining the time-resolved and HDR sequences. The left edge of the vector fields did not contain valid data due to low laser intensity in those regions. The lower half of the field of view also contained data of questionable validity due to low particle density and velocities. For these reasons the

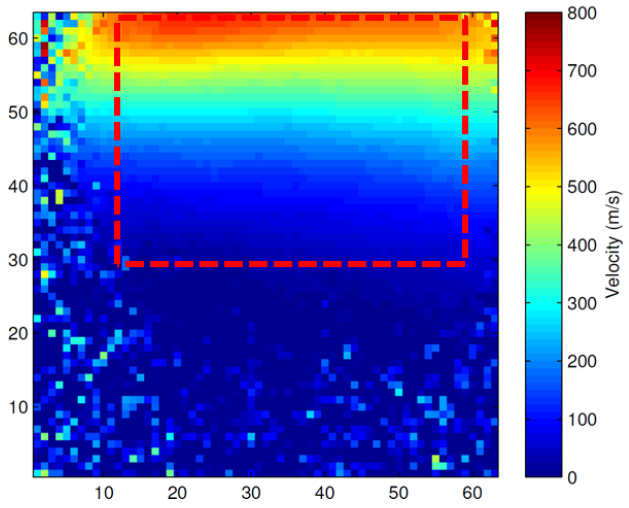

Figure 5.8: Ensemble average of PIV data indicating region of valid data

data was cropped to the boxed region containing vectors 13-56 in the x-direction and 30-63 in the y-direction.

5.2.1 Zero Displacement Correction

While the calibration steps taken above to align the cameras significantly reduced the errors associated misalignment of the eight camera frames, a zero displacement correction step was also applied to further improve the data quality. This process required raw images taken immediately following the completion of the experiment. 20 sequences of the jet flow were taken with each of the eight cameras simultaneously. The first exposure of the or the eight frames was taken at $t_0 = 0$ and the second exposure of each of the frames was taken at $t = t_0 + \Delta t$ where Δt was some unimportant time following the first exposure. This resulted in 40 sets of zero displacement images where each sequence of 16 images contained 2 sets of 8 images taken simultaneously. These zero displacement images were then processed and calibrated using the same steps outlined above. An average correlation of these images was then obtained using Dantec's Dynamic PIV software. The arrangement of the image pairs was done so that an average correlation was obtained for every possible camera combination. For example, an average correlation between cameras: 1:2, 1:3, 1:4, 1:5, 1:6, 1:7, 1:8, 2:3, all

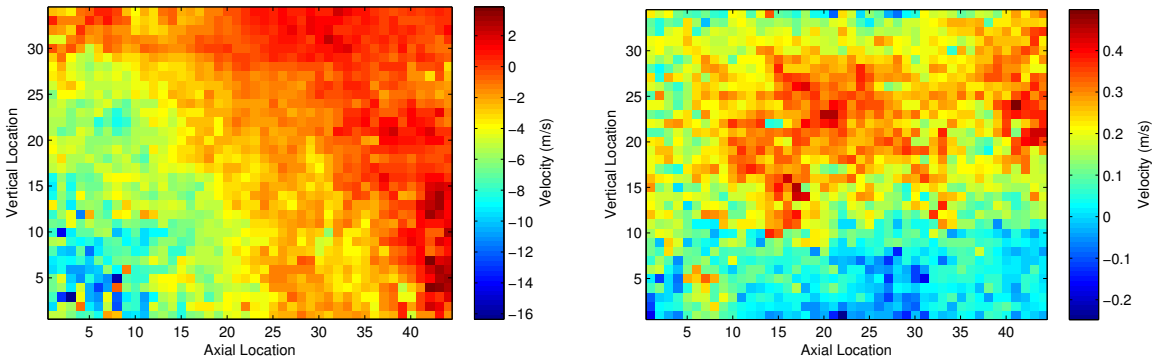

(a) u-component (b) v-component

Figure 5.9: Systematic error calculated from the average displacement of all zero displacement images

the way out to 7:8 was obtained. Each average was calculated using correlation of 40 image pairs. Because each image pair processed was simultaneously exposed, zero displacement should ideally be measured. However, because of the slight misalignment, a slight displacement between the frames was measured and quantified through the average correlation. This displacement represented the systematic error within the alignment of the PIV system for each of the camera combinations. During the PIV analysis of the experimental data, this systematic error was subtracted from the experimental vector fields, therefore removing it from the measurements. In order to represent the systematic error across each of the cameras, an average of all of the zero displacement combinations were averaged together and are shown in Figure 5.9. From Figure 5.9 it can be seen that the average systematic error measured in the axial direction is very low while the error in the vertical direction is much higher. The large magnitude of the error in the vertical direction indicates that the confidence in the accurate measurement of this component of velocity is should be low. Note that the field of view for both of these displacement fields has been cropped to the region believed to contain the most valid data as mentioned previously.

While the elimination of the systematic error through the subtraction of the zero-displacement combinations does eliminate some of the remaining error, it does not eliminate the truly random error within the system. This random error cannot be accounted for in the

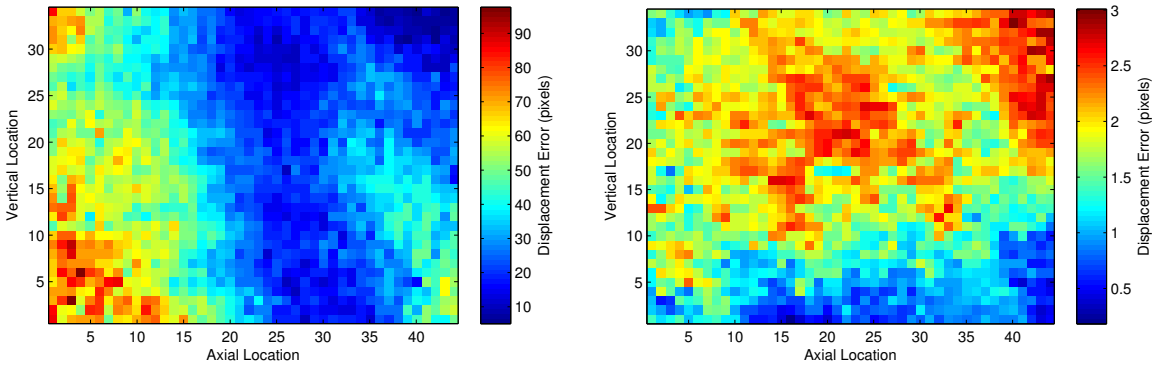

(a) u-component (b) v-component

Figure 5.10: Random error calculated from the standard deviation of all zero displacement images

same way as the systematic error by simple subtraction. Instead this error is random in nature, changing from frame to frame. The range of values in which this random error may fall however can be identified through the fluctuations of the zero-displacement images. This was done by calculating the standard deviation for all of the zero-displacement combinations and is shown in Figure 5.10. The units in Figure 5.10 are displayed in pixel displacement rather than velocity for easier comparison to other PIV systems. From Figure 5.10a it can be seen that relatively low error fluctuation exist for the much of the imaged region. However along the left hand side it can be seen that higher values of error fluctuations exist, particularly in the bottom left corner. These problems may still be due to the low particle seeding and laser intensity present in these regions of the field of view. In the axial direction, the overall uncertainty for the measurements falls between .1 and 3 pixels, with the majority of the values being close to .5 pixels. Figure 5.10b further confirms the earlier statement about the accuracy of the v-component measurements because large fluctuations in the random error exist in much of the imaged region and which will have a negative impact on the overall quality of results presented later in the chapter. For the overall uncertainty in the vertical direction, the values fall between .1 and 3 pixels, with the majority of the values being closer to 2 pixels.

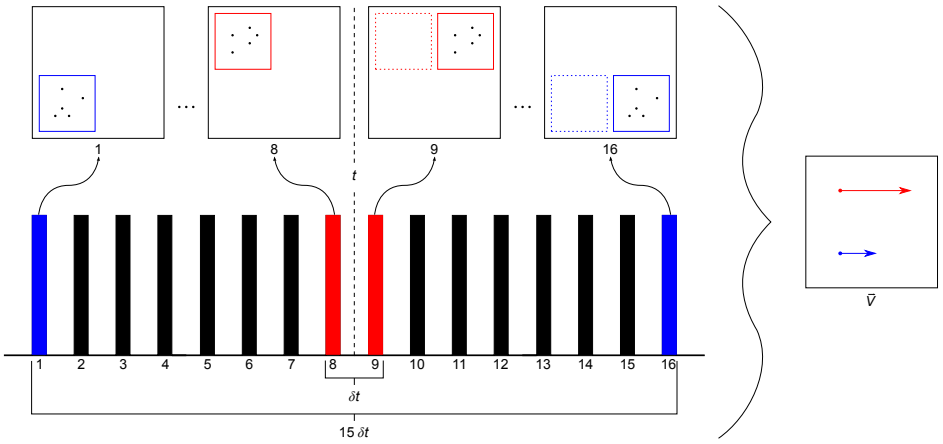

Figure 5.11: Sequence timing for Devols Algorithm[5]

5.2.2 High Dynamic Range PIV

Conventional PIV systems utilize two images acquired over a known time interval δt. This time interval is selected based on the velocity of the mean flow field and is generally set to allow for a particle to travel one-quarter of the length of the interrogation windows. This approach is adequate for the examination of most flow fields but in the case of turbulent jet shear layers where high velocity gradients exist, problems arise. While one region of the flow contains particles traveling the desired distance, other areas may travel only a fraction of that. This is acceptable if the desired data consists of large ensemble averages. However, in the case of this experiment, a time evolution of velocity fields is desired which requires additional steps to eliminate error within the PIV images. This can by done by implementing a multi-frame camera and using a high dynamic range algorithm to process the vector fields.

The HDR algorithm, dynamic evaluation via ordinary least squares (DEVOLS), was developed by Haynes[8] in the first year of the project and was used in the current work. The algorithm's purpose is to take image pairs previously processed through PIV software and to combine data at various δt's into a single velocity estimate. It utilizes symmetrically centered vector fields with increasing temporal spacing to calculate a single vector field. A timing schematic illustrating this can be seen in Figure 5.11. The algorithm utilizes only

the closest image pairs in regions experiencing high velocities. As the velocity decreases, more image pairs are considered in displacement calculation. The least squares method is used to fit a line between the increasing displacement values. Image pairs are eliminated until a specified RMS error is achieved. A more detailed explanation can be found in the following sources.[5, 8] This method however yields only one vector field rather than time resolved HDR sequences. In order to achieve this, the algorithm was modified so that the center time point varied between each image pair and correlations symmetric about these time locations were processed through DEVOLS. Vector fields near the beginning and end of the time sequence were only able to utilize two to four image pairs while middle of the sequence continued to consider every image pair. For example, when a center point between image 3 and 4 was considered, the corresponding image pairs utilized by the algorithm were 3-4, 2-5, and 1-6. It was determined that DEVOLS was not effective in a high dynamic range sense, but was very effective at eliminating invalid vectors which lead to increased accuracy in the final velocity field. A comparison of a single vector field, one processed using standard PIV and the other using DEVOLS algorithm can be seen in Figure 5.12. From these figures it can be seen that some of the spurious vectors existing within the flow field have been reduced or eliminated, improving the overall quality of the vector field. It is still clear from Figure 5.12b that significant variations and bad vectors remain. To address this problem, a further processing step was implemented in the form of POD reconstruction which is presented below.

5.2.3 Snapshot POD

The size of the data set, 308 sequences with a total of 4004 vector fields, allowed for the identification of the most common features within the flow field. This was accomplished through proper orthogonal decomposition, or POD. POD was first introduced by Lumley[56] in 1967 which provided a method for identifying coherent structures within a flow. The snapshot POD method implemented in this work was first introduced by Sirovich[57] in

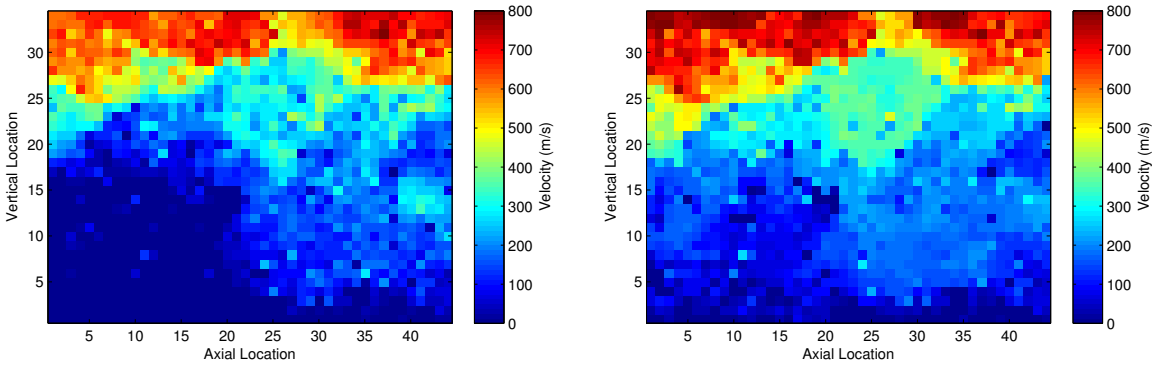

(a) standard PIV vector field

(b) Processed HDR vector field

Figure 5.12: Comparison of standard PIV result to the DEVOLS HDR result

1977 as a way of correlating instantaneous velocity fields within a flow. This method reduces the order of the eigen values to the number of snapshots within the data set rather than the number of data points.[58]

The modes within a data are identified within Snapshot POD by correlating the fluctuations of all the vector fields and constructing a covariance matrix C

$$C = \begin{bmatrix} u_1' \cdot u_1' & \cdots & u_1' \cdot u_n' \\ \vdots & \ddots & \vdots \\ u_n' \cdot u_1' & \cdots & u_n' \cdot u_n' \end{bmatrix}$$

where u' represents the fluctuating velocity and n is the number of vector fields within the data set. By then calculating the eigenvectors, α, and the eigenvalues, λ, of the covariance matrix, it can be shown the largest eigenvalues represent the modes with the highest turbulent kinetic energy. An example calculation for the first mode is shown below,

$$\phi_1 = \sum_{i=1}^{n} \alpha_{i1} u_i'$$

where ϕ_1 is the first mode. All the modes for every vector field can be calculated in this fashion and the energy (importance) of each corresponds to the magnitude of the eigenvalue.[58]

While this method could be applied to the entire data set, certain vector fields, and occasionally entire sequences, were eliminated due to their quality. Also because of problems the previously discussed associated to particle seeding and image distortion, the images were cropped. This prevented distortion within the modes due to image quality problems. This brought the total number of vector fields used in the POD calculation down to 3601. In order to maintain a continuous time set within each vector sequence, the eigenvalues for each vector field eliminated from the calculation was interpolated for using its neighboring vector fields. The first ten modes for the entire data sets for both the x and y-component can be viewed at the end of this section in Figures 5.16 and 5.17. The normalized modal energy for each mode is shown in Figure 5.13 where it can be seen that a very fast drop in energy exists in the modes. This means that common turbulent structures are present across most of the vector fields and they represent the bulk of the total kinetic energy within the flow.

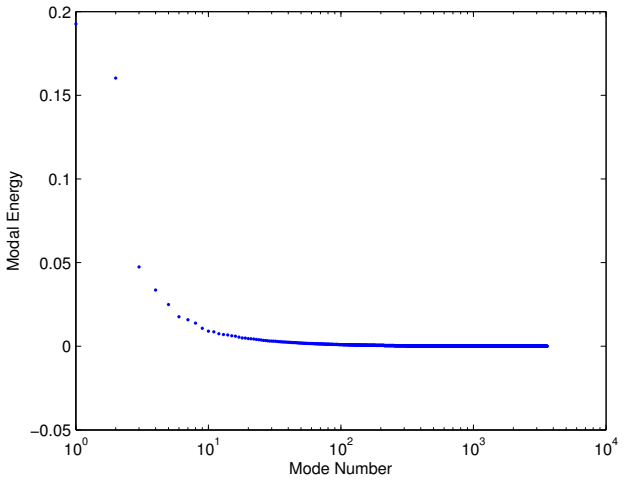

Figure 5.13: Modal Energy

While identifying most common turbulent features within the flow is beneficial, it is also possible to smooth, or eliminate noise from the vector fields using the calculated modes, or eigenvalue data. This is possible because any snapshot can be reconstructed as a linear combination of the POD modes and their eigenvalues. If every mode is utilized in the calculation, then the original vector field is obtained. However if the number of modes used

in the reconstruction are truncated based off of their contribution to the total modal energy, then the reconstructed vector field is smoothed of noise and spurious vectors. The equation below describes this process.

$$U_{new} = U_{avg} \sum_{i=1}^{m} \left(\frac{< u', \phi_i >}{< \phi_i, \phi_i} \right)$$

Identifying the number of modes to use in the reconstruction is done by calculating the the running sum of the normalized modal energy starting with the first mode. This can be seen graphically in Figure 5.14. There it can be seen again that the first modes make up the majority of the total kinetic energy. The number of modes used for the vector reconstruction in this work is identified by the 75% mark in Figure 5.14. This means that the first 110 modes made up 75% of the total energy which and were used in the reconstruction of vector fields.

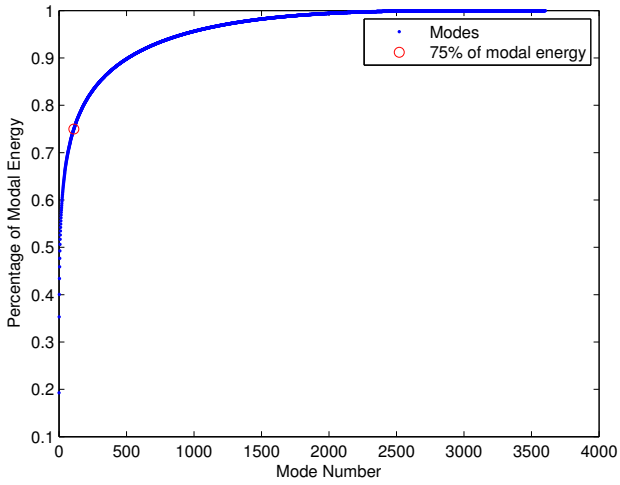

Figure 5.14: Sum of Normalized Modal Energy

The effectiveness of this method is displayed in Figure 5.15 where both the u and v components are reconstructed for a single vector field. The smoothing effect of the method can be clearly seen when comparing the original vector field to the reconstructed field. While the original quality of the v component is poor, the reconstruction does improve its quality

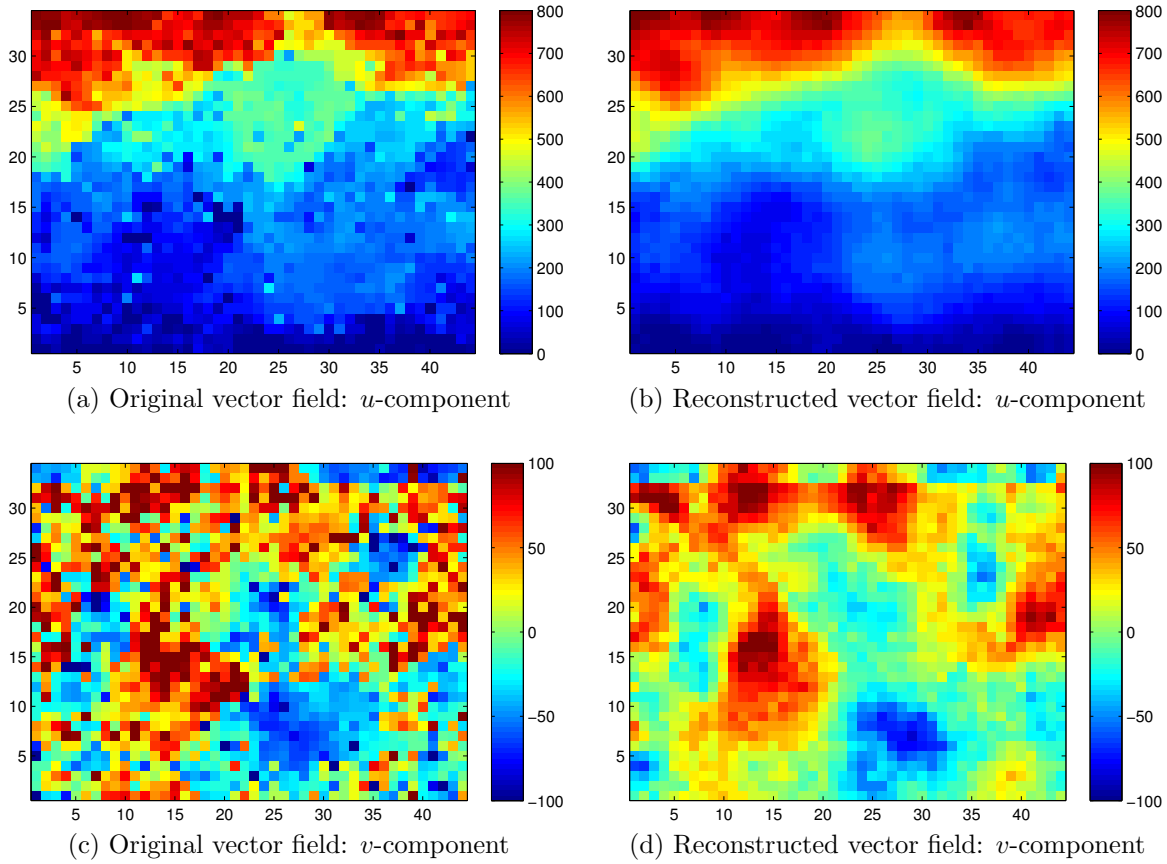

(a) Original vector field: u-component

(b) Reconstructed vector field: u-component

(c) Original vector field: v-component

(d) Reconstructed vector field: v-component

Figure 5.15: Comparison of original vector fields to POD reconstructed vector fields

drastically. This method was applied to all vector sequences for time resolved calculations which will be presented in the following chapter.

5.2.4 Polynomial Fits

In a final attempt to eliminate spurious vectors and decrease errors within the vector sequences, a polynomial fit was applied to each vector location within a vector field. Matlab's *polyfit* function was used to calculate one 2nd order polynomial fit at every vector location for each sequence. The RMS error for the initial fit was then calculated. If this RMS value was less 0.9, the outlying displacement vector was eliminated and the polynomial fit was re-calculated. This process was repeated until either the RMS error limit was achieved or 6 displacement values had been eliminated. This max number of iterations was imposed to ensure that each sequence retained it's time-resolved data. Figure 5.18 illustrates the process

detailed above by showing both the first and final iteration of the procedure. From this it is clear that the overall quality of the fit has been improved by eliminating the outlying vectors that appeared to be invalid.

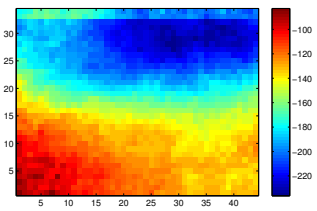

(a) Mode 1

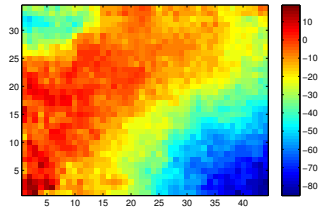

(b) Mode 2

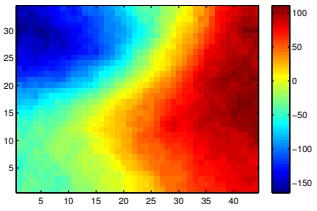

(c) Mode 3

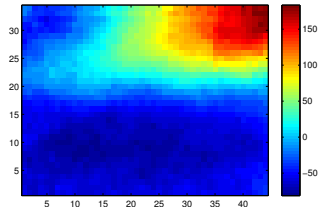

(d) Mode 4

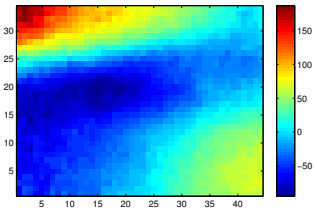

(e) Mode 5

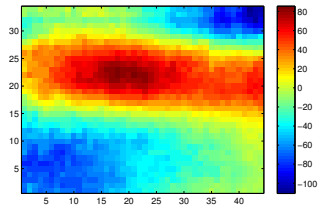

(f) Mode 6

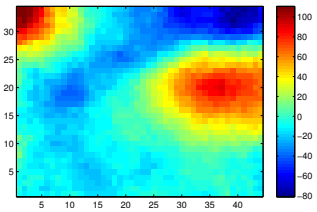

(g) Mode 7

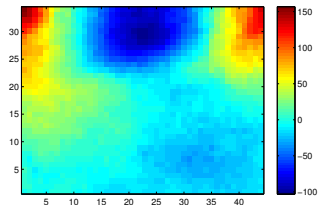

(h) Mode 8

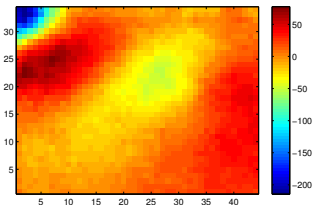

(i) Mode 9

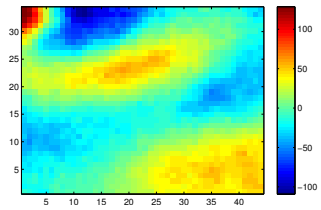

(j) Mode 10

Figure 5.16: POD modes for u-component of velocity

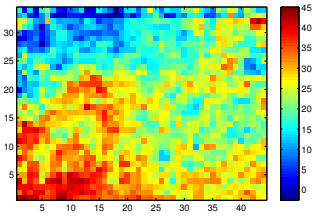

(a) Mode 1

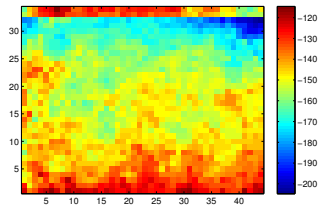

(b) Mode 2

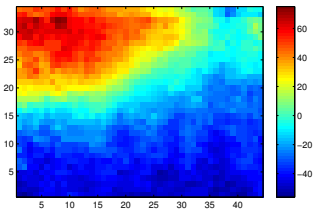

(c) Mode 3

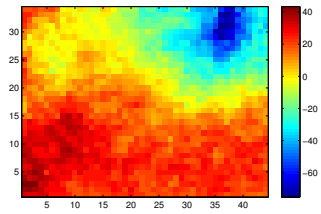

(d) Mode 4

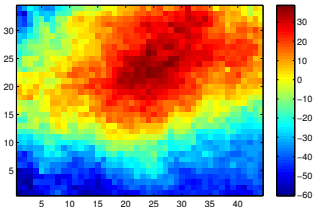

(e) Mode 5

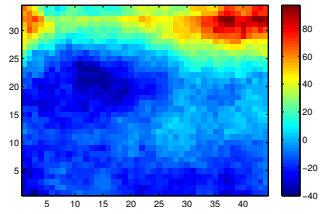

(f) Mode 6

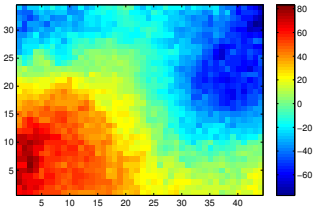

(g) Mode 7

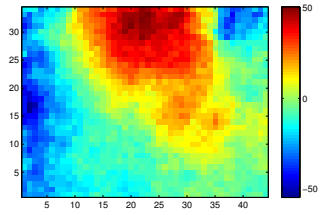

(h) Mode 8

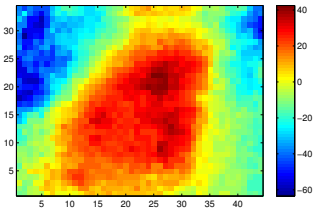

(i) Mode 9

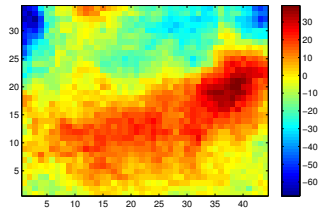

(j) Mode 10

Figure 5.17: POD modes for v-component of velocity

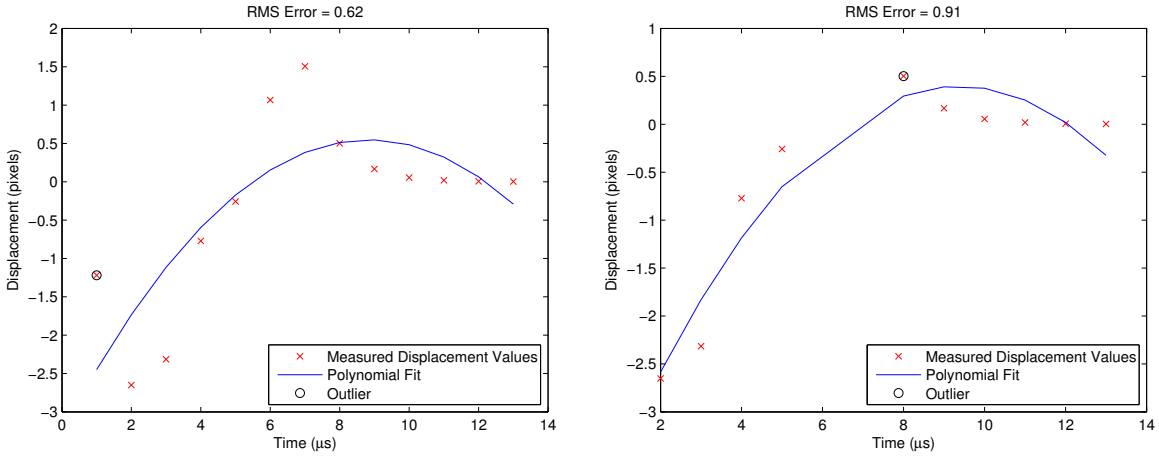

(a) Initial Iteration (b) Final Iteration

Figure 5.18: Displacement graphs used for the calculation of polynomial fits

Chapter 6

PIV Results

Utilizing the each step described in the previous chapter, all of the experimental images and resulting vector fields were processed in order to obtain the most accurate results possible from the gathered data which are presented below. This includes the application of DEVOLS algorithm, POD reconstruction as well as the polynomial fits. Despite these efforts, the quality of the initial data allowed only for the presentation of primarily averaged PIV data with the inclusion of only a couple of time-resolved sequences. The shortcomings of the data will be discussed in more depth later in this chapter and in the conclusion.

The average velocity fields for the u and v components as well as the ensemble average of the fluctuating velocity fields u', v' and $u'v'$ were calculated and can be seen in Figures 6.1-6.4. From Figure 6.1a it can be seen that the high velocity region within the jet's core was captured as well as the shear layer. The magnitude of the velocity is close to 700 m/s in the axial direction at the jets core and is consistent with the location of measurement and the operating conditions of the facility. This can clearly be seen in the in the vertical velocity slice taken from the average u-component of velocity shown in Figure 6.2. It is important to note that much of the imaged flow field contains very low velocity. This indicates that the selected image region could have shifted higher up to encompass more of the jet's core flow as was mentioned previously. The effects of the fluctuating shear layer can be seen in the top of Figure 6.1b where larger velocity fluctuations are present with values consistently near 150 m/s. However the corners of these regions contain very high velocity fluctuations, greater than 200 m/s, due to low particle density, diminished laser intensity and image distortions. This is particularly evident in the top right of Figure 6.1b where the effect of image distortion was greatest and could not be corrected through image processing.

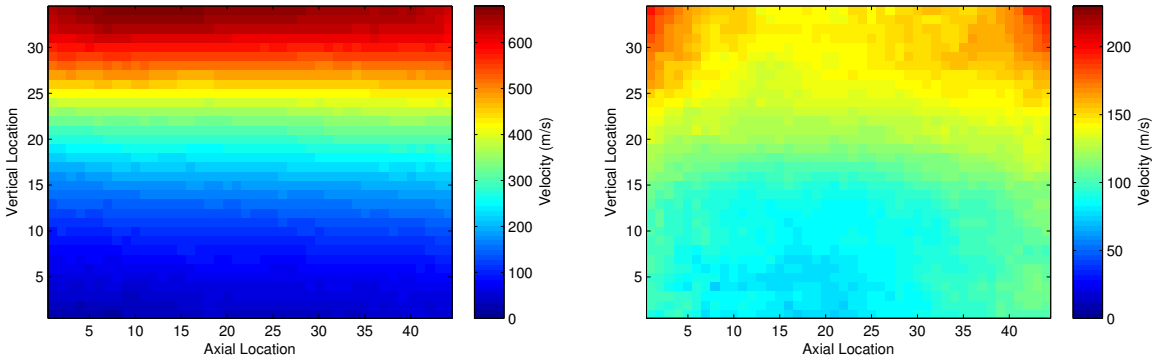

(a) Average u velocity component (b) Fluctuating velocity u'

Figure 6.1: Average HDR velocity fields for u component

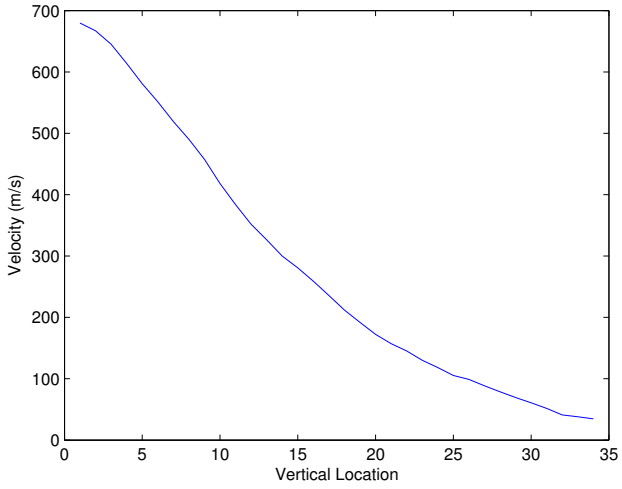

Figure 6.2: Velocity slice in the vertical direction for the average u-component of velocity

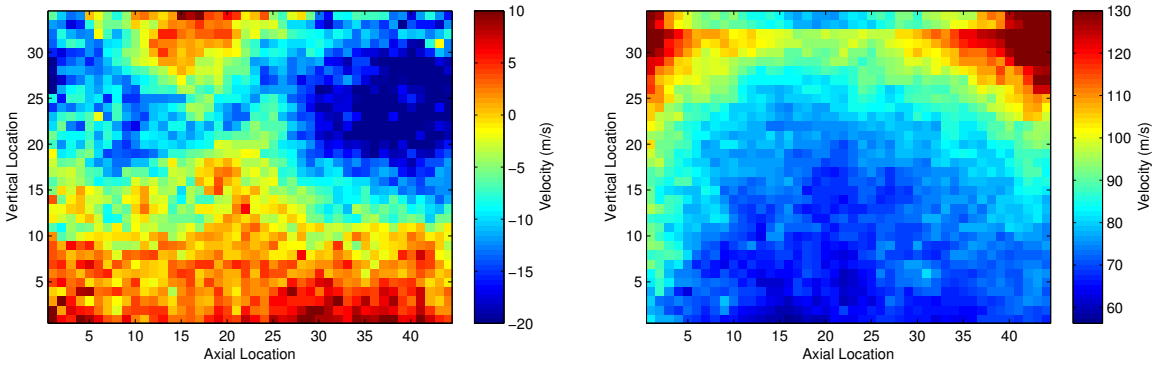

(a) Average v velocity component

(b) Fluctuating velocity v'

Figure 6.3: Average HDR velocity fields for v component

The vertical velocity components shown in Figure 6.3a were very low as expected within this flow field, with a maximum velocity of 10 m/s and a minimum of -20 m/s. The location of the positive vertical velocity corresponds to the edge of the shear layer where flow is being entrained into the high speed jet flow. While Figure 6.3a shows the velocity, the maximum displacement measured was less than 1 pixel.

Finally the average velocity magnitude is shown in Figure 6.4. Figure 6.4a shows the flow field in vector form with the color bar indicating velocity magnitude. As expected the velocity magnitude is very similar to the axial component of velocity shown in Figure 6.1a with an average core velocity near 700 m/s and a velocity differential through the shear layer of around 600 m/s. The Reynolds stress calculation shown in Figure 6.4b indicates that momentum is being transferred from the jet core into the entrained flow. The due to the negative $u'v'$ values within the shear layer.

The average vorticity field is shown in Figure 6.5. It was calculated using the least squares method. While this allowed for smoother result, it decreased the field of view by two vector spaces on each side of the field.

6.1 Velocity Sequences

Because the data was processed through DEVOLS algorithm in such a way as to maintain the time correlations between the velocity fields, the time evolution of a vector field

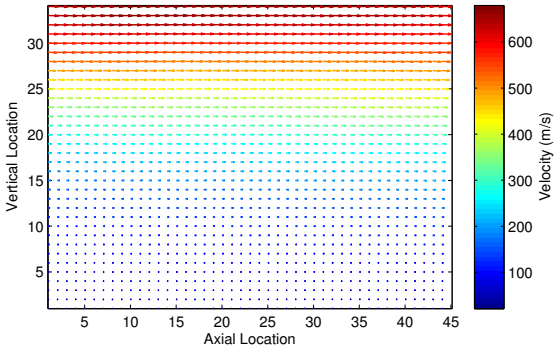

(a) Average velocity vectors

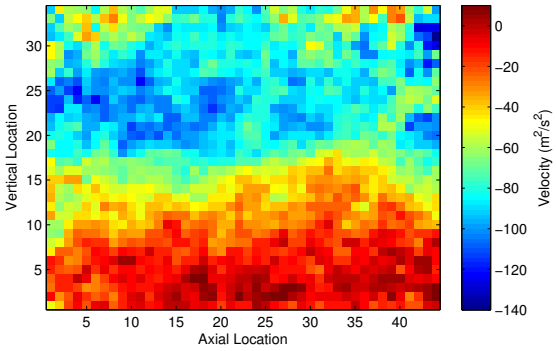

(b) Average Reynolds Stress $u'v'$

Figure 6.4: Average HDR velocity fields for uv component

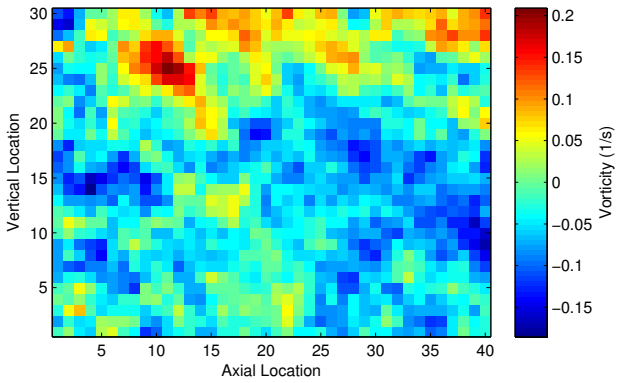

Figure 6.5: Average vorticity field

within a sequence could still be calculated. The use of the 2nd order polynomial fit discussed in the previous chapter allowed for further smoothing of the velocity sequence. The effects of this were of particular use for the examination of velocity sequences. This is because the dominant features present in the velocity sequences were maintained while the smoothing effect of the polynomial fit eliminated the fluctuations of spurious vectors. As previously stated the temporal spacing between each image of the velocity sequences is 1 μs.

The first velocity sequence is shown in Figure 6.6 where it can be seen that a region of low speed flow within the shear layer is impinging on the high speed layer of the flow. This turbulent structure is approximately 14.7 mm in length and 9.9 mm in height. With the progression of time the low speed region appears to progress down stream in the flow field a length of 5.8 mm. This gives the structure an approximate velocity of 418 m/s. This could be a vortex within the shear layer interacting with the high speed core of the jet flow. There were not enough time-resolved sequences in the ensemble to compute statistics and form conclusions on the space-time evolution of the turbulence. Furthermore, the sample rate was evidently higher than necessary to examine the temporal development of the shear layer structures.

Another velocity sequence can be seen in Figure 6.7. Similar to the sequence in Figure 6.6, Figure 6.7 contains a low speed flow region impinging upon the high speed flow. However here the effects are more drastic with the low speed region pushing the jet core almost entirely out of the image region. The size of the structure is approximately 21.6 mm and 9.9 mm in length and height respectively. As the sequence progresses, this area propagates downstream a distance of approximately 6.9 mm, protruding further into the core flow. This gives the structure an approximate velocity of 525 m/s. Near the sequence's end, the low speed bulge seems to roll up into the core, with a high speed region protruding down at the edge of the bulge. This again demonstrates the affect of the turbulent shear layer on the jet core. While only two velocity sequences are shown, they do show the turbulent nature of the flow and the

capability of high speed time resolved data to enhance our understanding of the turbulent features present within supersonic jets.

6.2 Acceleration Data

The average acceleration components as well as their fluctuating quantities can be seen in Figures 6.8-6.9. While significant effort was made to eliminate error wherever possible including HDR analysis, POD reconstruction, vector elimination, and the use of the polynomial fits, it is clear from these figures that little can be learned from the acceleration data. This is possibly due to poor particle seeding, or more likely residual noise and jitter that remained after the image processing steps described above.

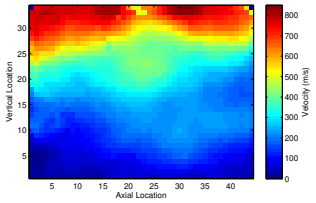

(a) 1

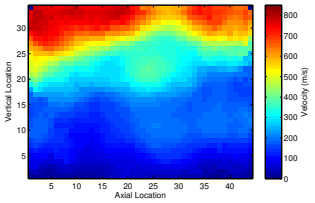

(b) 7

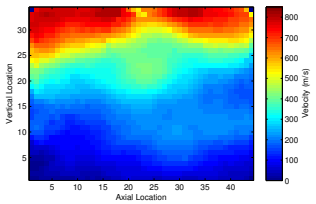

(c) 2

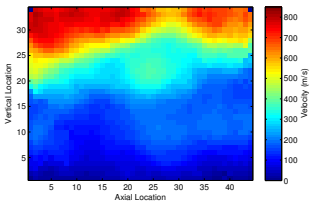

(d) 8

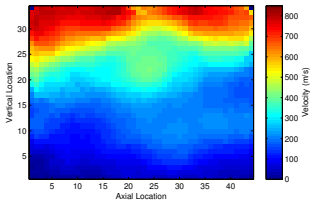

(e) 3

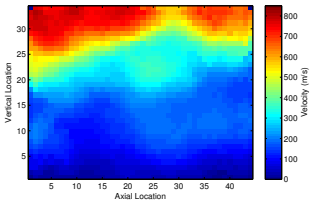

(f) 9

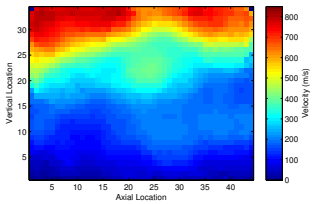

(g) 4

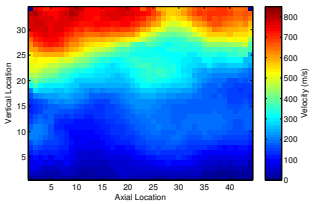

(h) 10

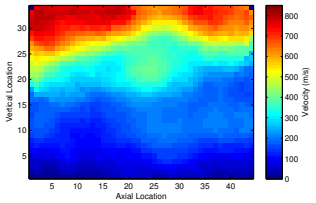

(i) 5

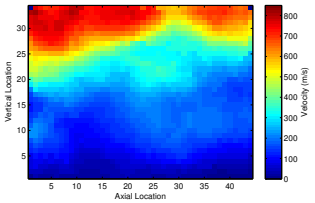

(j) 11

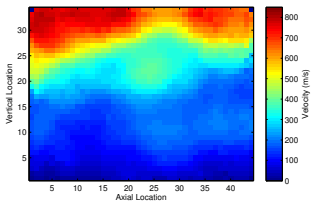

(k) 6

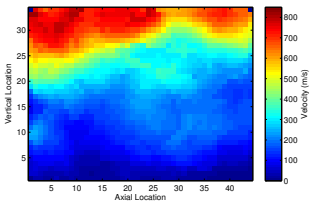

(l) 12

Figure 6.6: Time-resolved velocity sequence

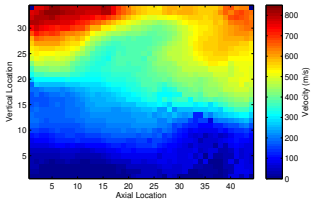

(a) 1

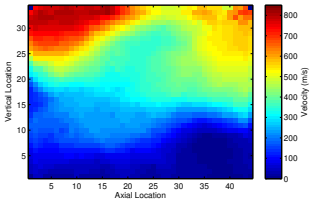

(b) 7

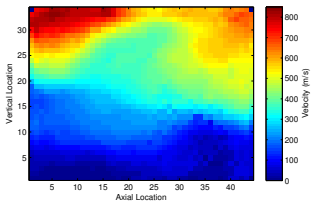

(c) 2

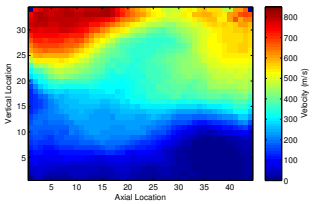

(d) 8

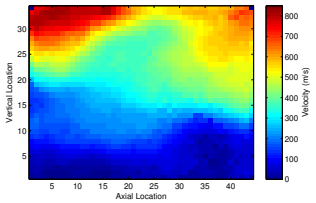

(e) 3

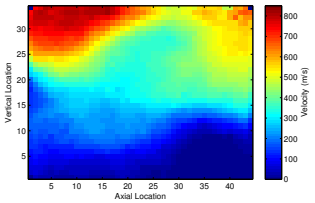

(f) 9

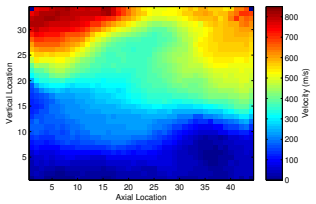

(g) 4

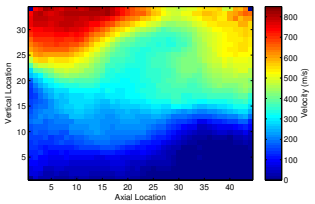

(h) 10

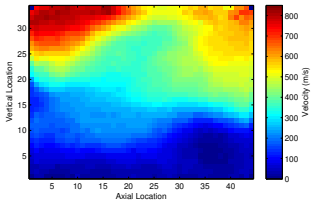

(i) 5

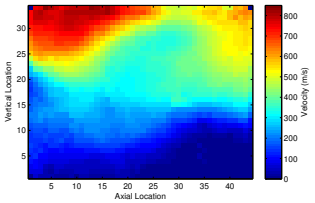

(j) 11

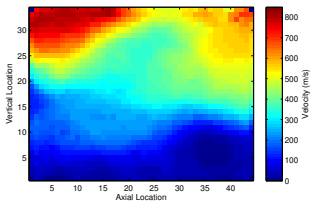

(k) 6

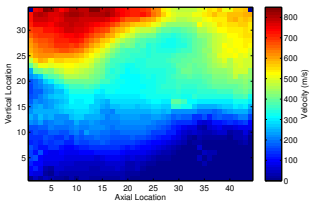

(l) 12

Figure 6.7: Time-resolved velocity sequence

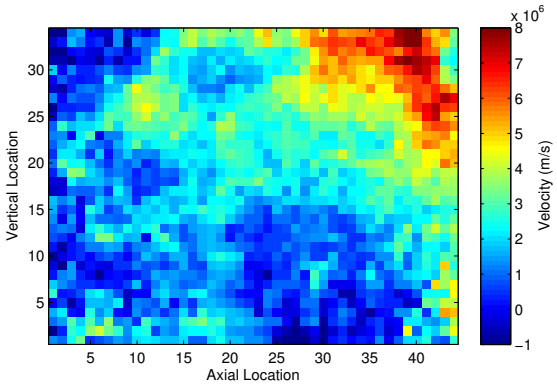

(a) Average $\frac{\partial u}{\partial t}$ acceleration component

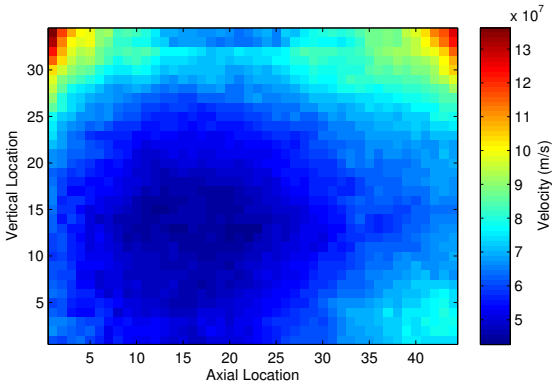

(b) Fluctuating acceleration for $\frac{\partial u}{\partial t}$

Figure 6.8: Average HDR acceleration fields for u component

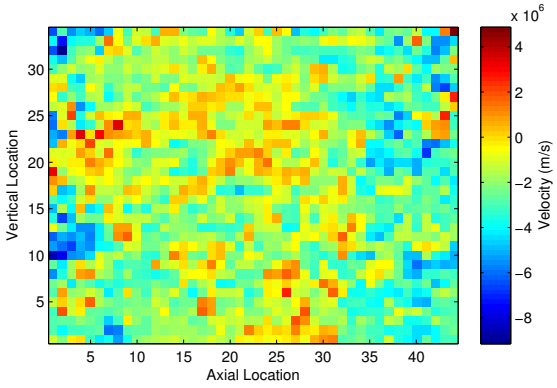

(a) Average $\frac{\partial v}{\partial t}$ acceleration component

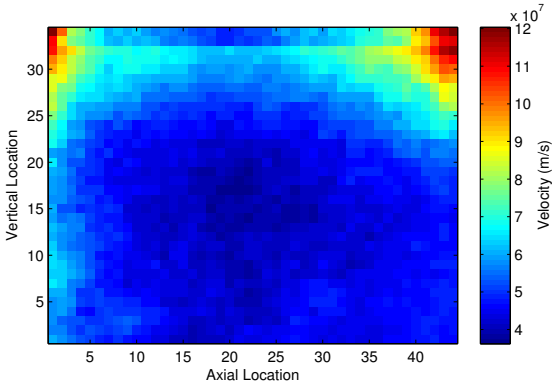

(b) Fluctuating acceleration for $\frac{\partial v}{\partial t}$

Figure 6.9: Average HDR acceleration fields for v component

Chapter 7

Concluding Remarks

The use of MHz rate time resolved PIV was been demonstrated on a heated supersonic jet. Due to various problems including image quality and low particle density, additional processing steps had to be taken to improve the final data. While these measures did mitigate some of these issues, they did not eliminate them. It is apparent that the use of the Cordin gate intensified framing CCD camera, while allowing for high speed image acquisition, did introduce significant complications in the form of random MCP noise, camera jitter, and low image intensity. The persistent camera blurring due to acoustic vibrations also remained. Future experimental attempts will pursue alternative means for image acquisition.

While time resolved velocity sequences were presented, the persistent problems listed above have prevented the use of acceleration data for the calculation of Lighthill's stress tensor. Despite these problems, MHz rate PIV on a supersonic jet was conducted and analyzed which has not been possible through conventional PIV. It had been the hope the the synchronization of the near and far-field pressure data could be correlated with the time-resolved velocity fields and acceleration fields. This could in turn be used to help calculate the noise sources within the turbulent jet. While it was found that the use of DEVOLS algorithm, POD reconstruction as well as polynomial fits were able to improve the overall quality of the vector fields they were unable overcome the poor data quality associated with the Cordin camera. This in-turn prevented a more detailed and in depth aeroacoustic analysis from being included in this paper. However while the current system did not provide adequate data, it has been demonstrated that MHz PIV is feasible and shows promise in furthering our fundamental knowledge regarding the production of sound within a supersonic jet.

Bibliography

[1] Fahy, F., *Foundations of Engineering Acoustics*, Academic Press, Amsterdam, 2001.

[2] Tam, C. K. W., "Supersonic Jet Noise," *Annual Review of Fluid Mechanics*, Vol. 27, No. 1, Jan. 1995, pp. 17–43.

[3] Murray, N., Tinney, C., Thurow, B., Haynes, H., and Panickar, P., "A Laboratory Framework for Synchronous Near/Far-Field Acoustics and MHZ PIV in High-Temperature, Shock-Containing, Jets," No. 1270, ASME, New York, August 2012.

[4] Raman, G., "SUPERSONIC JET SCREECH : HALF-CENTURY FROM POWELL TO THE PRESENT," *Journal of Sound and Vibration*, Vol. 225, No. 3, 1999, pp. 543–571.

[5] Haynes, R. H., Brock, B. A., and Thurow, B. S., "Application of MHz Frame Rate, High Dynamic Range PIV to a High-Temperature, Shock-Containing Jet," *Aerospace Science Meeting*, 2012.

[6] Cordin Company, *Cordin 222-4g Gated Intensified CCD Framing Camera User Manual*, 2011.

[7] Roger, M., "Fundamentals of aero-acoustics," *Applied Aero-Acoustics: Prediction Methods*, Vol. 4 of *Lecture Series*, von Karman Institute, Saint Genese, Belgium, 1996, pp. 1–30.

[8] Haynes, R. H., Brock, B. A., and Thurow, B. S., "Application of MHz frame rate , high dynamic range PIV to a high-temperature , shock-containing jet," *AIAA*, 2013, pp. 1–21.

[9] Lighthill, M. J., "On Sound Generated Aerodynamically. I. General Theory," *Proceedings of the Royal Society A: Mathematical, Physical and Engineering Sciences*, Vol. 211, No. 1107, March 1952, pp. 564–587.

[10] Russell, D. A., Titlow, J. P., and Bemmen, Y.-j., "Acoustic monopoles, dipoles, and quadrupoles: An experiment revisited," *American Journal of Physics*, Vol. 67, No. August, 1999, pp. 660–664.

[11] Barlow, J. B., William H. Rae, J., and Pope, A., *Low-Speed Wind Tunnel Testing*, Wiley Interscience, New York, 3rd ed., 1999.

[12] Juve, D., "Aeroacoustics: From Fluid Dynamics To Acoustics," *Aeroacoustics and Active Noise Control*, Lecture Series, von Karman Institute, 1997, pp. 1–27.

[13] List, E. J., "Turbulent Jets and Plumes," *Journal of Fluid Mechanics*, Vol. 14, 1982, pp. 182–212.

[14] Howe, M. S., *Hydrodymanics and Sound*, Cambridge, New York, 2007.

[15] Lighthill, S. J., "Some Aspects of the Aeroacoustics of High-Speed Jets," *ICASE*, 1993.

[16] Kandula, M. and Vu, B., "ON THE SCALING LAWS FOR JET NOISE IN SUBSONIC AND SUPERSONIC FLOW," Tech. rep., 2003.

[17] Sutherland, L. C., "Progress and problems in rocket noise prediction for ground facilities," *15 AIAA Aeroacoustics Conference*, October 1993.

[18] Tam, C. K., Pastouchenko, N. N., and Viswanathan, K., "Fine-Scale Turbulence Noise from Hot Jets," *AIAA Journal*, Vol. 43, No. 8, Aug. 2005, pp. 1675–1683.

[19] Seiner, J. and Norum, T., "Measurements of the Mean Static Pressure and Far-Field Acoustics of Shock-Containing Supersonic Jets," Tech. rep., National Aeronautics and Space Administration, 1982.

[20] Powell, A., "On the Mechanism of Choked Jet Noise," *Proceedings of Physical Society of London*, Vol. 66, 1953, pp. 1039–1056.

[21] Tam, C. K. W., *Aeroacoustics of Flight Vehicles: Theory and Practice*, Vol. 1, chap. 6) Noise Generated by Large-Scale Coherent Motion, NASA, 1991, pp. 311–384.

[22] Thurow, B. S., Jiang, N., and Lempert, W., "Review of ultra-high repetition rate laser diagnostics for fluid dynamic measurements," *Measurement Science and Technology*, Vol. 24, No. 1, Jan. 2013, pp. 012002.

[23] Stainback, P. C. and Nagabushana, K. A., "Review of Hot-Wire Anemometry Techniques and the Range of their Applicability for Various Flows," *Journal of Fluids Engineering*, 1996.

[24] Bridges, J. E. and Wernet, M. P., "Turbulence Associated With Broadband Shock Noise in Hot Jets," Tech. Rep. September, NASA, 2008.

[25] Wernet, M. P. and Opalski, A. B., "Development and Application of MHz Frame Rate Digital Particle Image Velocimetry System," *24th AIAA Aerodynamic Measurement Technology and Ground Testing Conference*, 2004.

[26] Murphy, M. J. and Adrian, R. J., "PIV space-time sesolution of flow behind blast waves," *Experimental Fluids*, Vol. 49, 2010, pp. 193–202.

[27] Tedder, S. and Hicks, Y., "OH Planar Laser Induced Fluorescence (PLIF) Measurements for the Study of High Pressure Flames : An Evaluation of a New Laser and a New Camera System," Tech. Rep. May, NASA, 2012.

[28] Kaminski, C. F., Hult, J., and Ald, M., "High repetition rate planar laser induced fluorescence of OH in a turbulent non-premixed flame," *Applied Physics*, Vol. 760, 1999, pp. 757–760.

[29] Sjoholm, J., Kristensson, E., Richter, M., Alden, M., Goritz, G., and Knebel, K., "Ultra-high-speed pumping of an optical parametric oscillator (OPO) for high-speed laser-induced fluorescence measurements," *Measurement Science and Technology*, Vol. 20, 2009.

[30] Jiang, N. and Lempert, W. R., "Ultra-high frame rate nitric oxide planar laser induced fluorescence imaging," *Optics Letters*, Vol. 33, 2008, pp. 2236–2238.

[31] Jiang, N., Webster, M., Lempert, W., Miller, J. D., Meyer, T. R., Ivey, C. B., and Danehy, P. M., "MHz-rate NO PLIF imaging in a Mach 10 hypersonic wind tunnel," *Applied Optics*, Vol. 50, 2011.

[32] Thurow, B. S., Jiang, N., Lempert, W. R., and Samimy, M., "Development of Megahertz-Rate Planar Doppler Velocimetry for High Speed Flows," *AIAA*, Vol. 43, No. 3, March 2005, pp. 500–511.

[33] Laufer, J., Schlinker, R., and Kaplan, E., "Experiments on Supersonic Jet Noise," *AIAA Journal*, Vol. 14, 1976.

[34] Billingsley, J. and Kinns, R., "The Acoustic Telescope," *Journal of Sound and Vibration*, Vol. 48, 1976, pp. 485–510.

[35] Humphreys, W. M., Brooks, T. F., Hunter, W. W., and Meadows, K. R., "Design and Use of Microphone Directional Arrays for Aeroacoustic Measurements & Exhibit," *36st Aerospace Sciences Meeting*, 1998.

[36] Narayanan, S., Barber, T. J., and Polak, D. R., "High Subsonic Jet Experiments: Turbulence and Noise Generation Studies," *AIAA Journal*, Vol. 40, 2002, pp. 430–437.

[37] Hileman, J., Thurow, B. S., and Samimy, M., "Exploring Noise Sources Using Simultaneous Acoustic Measurements and Real-Time Flow Visualizations in Jets Introduction," *AIAA Journal*, Vol. 40, 2002.

[38] Hileman, J., Thurow, B., and Samimy, M., "Development and evaluation of a 3-D microphone array to locate individual acoustic sources in a high-speed jet," *Journal of Sound and Vibration*, Vol. 276, No. 3-5, Sept. 2004, pp. 649–669.

[39] Hileman, J., Thurow, B. S., Caraballo, E. J., and Samimy, M., "Large-scale structure evolution and sound emission in high-speed jets: real-time visualization with simultaneous acoustic measurements," *Journal of Fluid Mechanics*, Vol. 544, No. -1, Nov. 2005, pp. 277.

[40] Papamoschou, D. and Dadvar, A., "Localization of multiple types of noise sources," *12th AIAA/CEAS Aeroacoustics Conference*, 2006.

[41] Venkatesh, S. R., Polak, D. R., and Narayanan, S., "Beamforming Algorithm for Distributed Source Localization and Its Application to Jet Noise," *AIAA Journal*, Vol. 41, 2003.

[42] Baars, W. J., Tinney, C. E., Murray, N. E., Jansen, B. J., and Panikar, P., "The Effect of Heat on Turbulent Mixing Noise in Supersonic Jets," *49th AIAA Aerospace Sciences Meeting*, Orlando, Florida, January 2011.

[43] Norum, T. D. and Seiner, J. M., "Broadband Shock Noise from Supersonic Jets," *AIAA Journal*, Vol. 20, No. 1, 1982, pp. 68–73.

[44] Tam, C. K. W., "Stochastic model theory of broadband shock associated noise from supersonic jets," *Journal of Sound and Vibration*, Vol. 116, No. 2, 1987, pp. 265–302.

[45] Poldervaart, L. J., Vink, A. T., and Wijnands, A. P. J., "The photographic evidence of the feedback loop of a two dimensional screeching supersonic jet of air." *Proceedings of the 6th International Congress on Acoustics*, Tokyo, Japan 1968.

[46] Poldervaart, L. J., Wijnands, P. J., and Bronkhorst, I., "Film reviews," *Journal of Fluid Mechanics*, Vol. 78, No. 4, Oct. 1976, pp. 859–862.

[47] Tam, C. K., "Proposed relationship between broadband shock associated noise and screech tones," *Journal of Sound and Vibration*, Vol. 110, 1986, pp. 309–321.

[48] Panda, J., "An experimental investigation of screech noise generation," *Journal of Fluid Mechanics*, Vol. 378, Jan. 1999, pp. 71–96.

[49] Panda, J. and Seasholtz, R. G., "Measurement of shock structure and shockvortex interaction in underexpanded jets using Rayleigh scattering," *Physics of Fluids*, Vol. 11, No. 12, 1999, pp. 3761.

[50] André, B., Castelain, T., and Bailly, C., "Shock-Tracking Procedure for Studying Screech-Induced Oscillations," *AIAA Journal*, Vol. 49, No. 7, July 2011, pp. 1563–1566.

[51] Adrian, R. J. and Westerweel, J., *Particle Image Velocimetry*, Cambridge University Press, 2011.

[52] Thurow, B. S., Satija, A., and Lynch, K. P., "Third-generation megahertz-rate pulse burst laser system." *Applied optics*, Vol. 48, No. 11, April 2009, pp. 2086–93.

[53] Thurow, B., Satija, A., and Lynch, K., "Third-generation Megahertz-Rate Pulse Burst Laser System." *Applied Optics*, Vol. 48, 2009, pp. 2086–2093.

[54] Haynes, R. H., *Development of a High Dynamic Velocity Range Processing Scheme for Time-Resolved Particle Image Velocimetry Measurements*, Master's thesis, Auburn University, August 2013.

[55] Wernet, J. H. and Wernet, M. P., "Stabilized Alumina/Ethanol Colloidal Dispersion for Seeding High Temperature Air Flows," *Proceedings of the ASME Symposium on Laser Anemometry: Advances and Applications*, Lake Tahoe, NV, June 1994.

[56] Lumley, J. L., "The structure of inhomogeneous turbulent flows," *Atmospheric turbulence and radio wave propagation*, 1967, pp. 166–178.

[57] Sirovich, L., "Turbulence and the dynamics of coherent structures. Part I: Coherent structures," *Quaterly of Applied Mathmatics*, Vol. 45, 1977, pp. 561–571.

[58] Melnick, M. B., Thurow, B. S., and Hall, D., "On the Relationship Between Image Intensity and Velocity in a Turbulent Boundary Layer Seeded with Smoke Particles," , pp. 1–17.